



Systemically targeting monocytic myeloid-derived suppressor cells using dendrimers and their cell-level biodistribution kinetics

Chad A. Littrell^a, Gregory P. Takacs^a, Chenikkayala Siva Sankara^b, Alexandra Sherman^a, Kai A. Rubach^b, Julia S. Garcia^a, Coral A. Bell^b, Tejashwini Lnu^c, Jeffrey K. Harrison^a, Fan Zhang^{a,b,c,*}

^a Department of Pharmacology & Therapeutics, University of Florida College of Medicine, Gainesville, FL, United States

^b Department of Pharmaceutics, University of Florida College of Pharmacy, Gainesville, FL, United States

^c Department of Chemical Engineering, University of Florida College of Pharmacy, Gainesville, FL, United States

ARTICLE INFO

Keywords:

M-MDSC
PAMAM dendrimer
Biodistribution
CCR2
Glioblastoma
Cell uptake
Protein corona

ABSTRACT

The focus of nanoparticles *in vivo* trafficking has been mostly on their tissue-level biodistribution and clearance. Recent progress in the nanomedicine field suggests that the targeting of nanoparticles to immune cells can be used to modulate the immune response and enhance therapeutic delivery to the diseased tissue. In the presence of tumor lesions, monocytic-myeloid-derived suppressor cells (M-MDSCs) expand significantly in the bone marrow, egress into peripheral blood, and traffic to the solid tumor, where they help maintain an immunosuppressive tumor microenvironment. In this study, we investigated the interaction between PAMAM dendrimers and M-MDSCs in two murine models of glioblastoma, by examining the cell-level biodistribution kinetics of the systemically injected dendrimers. We found that M-MDSCs in the tumor and lymphoid organs can efficiently endocytose hydroxyl dendrimers. Interestingly, the trafficking of M-MDSCs from the bone marrow to the tumor contributed to the deposition of hydroxyl dendrimers in the tumor. M-MDSCs showed different capacities of endocytosing dendrimers of different functionalities *in vivo*. This differential uptake was mediated by the unique serum proteins associated with each dendrimer surface functionality. The results of this study set up the framework for developing dendrimer-based immunotherapy to target M-MDSCs for cancer treatment.

1. Introduction

Nanoparticles have been extensively used to deliver therapeutic payloads for disease treatment. While most *in vivo* biodistribution studies of nanoparticles have been focused on their tissue-level accumulation and clearance [1,2], recent progress in the nanomedicine field suggested that targeting nanoparticles to immune cells can be used to modulate the immune response and to enhance therapeutic delivery to the disease region [3–5].

For example, monocytic-myeloid-derived suppressor cells (M-MDSCs) are important cellular targets in cancer [6]. M-MDSCs are pathologically activated immature monocytes with potent immunosuppressive activities. Clinically, a high burden of M-MDSCs is associated with poor prognosis of many solid tumors [7]. In cancer, M-MDSCs help create and maintain an immunosuppressive tumor microenvironment (TME) [8,9]. These cells can suppress anti-tumor T cells and

promote regulatory T cells and anti-inflammatory myeloid cells [8,9]. As such, there is an urgent need to develop delivery strategies to target M-MDSCs for cancer treatment.

In addition to their immunosuppressive features, M-MDSCs, as phagocytes [10,11], could also significantly affect the *in vivo* fate of nanoparticles. Historic studies have established the critical roles of myeloid cells in clearing nanoparticles [12,13], while emerging evidence has shown that myeloid cells in circulation can take up nanoparticles and actively transport them to the inflamed tissue [4,14,15]. M-MDSCs are significantly elevated in the peripheral blood of high-grade glioblastoma patients, accounting for as much as 10% of total cells in the peripheral blood and 30% of total peripheral blood mononuclear cells [16,17]. In the presence of tumor lesions, the bone marrow accelerates monopoiesis and enhances the egress of M-MDSCs to the systemic circulation, leading to significant expansion of their population in the peripheral blood and in the spleen [18]. Tumors constantly recruit

* Corresponding author at: Department of Pharmaceutics, College of Pharmacy, University of Florida, Gainesville, FL, United States.

E-mail address: fzhang1@ufl.edu (F. Zhang).

<https://doi.org/10.1016/j.jconrel.2024.08.003>

Received 4 April 2024; Received in revised form 29 July 2024; Accepted 2 August 2024

Available online 15 August 2024

0168-3659/Published by Elsevier B.V.

M-MDSCs in large amounts through CCR2-mediated chemotaxis to replenish the tumor-associated macrophages (TAMs) [19,20]. The abundance of M-MDSCs and their constant infiltration to the tumor sites highlights the potential of M-MDSCs in mediating nanoparticle deposition at the tumors.

Given the important roles of M-MDSCs in establishing the TME and mediating nanoparticle tumor-targeting, many efforts have tried to establish the correlation between nanoparticle physicochemical properties, such as size, surface charge, and surface ligands to their targeting of M-MDSCs [21–24]. However, a critical challenge in studying the cell targeting behaviors of nanoparticles is that when nanoparticles are injected into the blood, multiple serum proteins such as immunoglobulins, fibrinogen, complement proteins, and apolipoproteins readily adsorb to the nanoparticle surface, forming a ‘protein corona’ [25,26]. The protein corona masks the native nanoparticle interactions with the cell surface and alters the nanoparticle’s cellular tropism [25,26]. It is now recognized that nanoparticle-associated proteins dictate nanoparticle interactions with cells and, more broadly, their *in vivo* targeting behaviors. The physical properties of nanoparticles only play a secondary role in this process.

Dendrimers represent a class of ultra-small nanoparticles with sub-10 nm size that carry drug payload on their surface. About 26 dendrimer-based therapeutics with various types of payloads are currently under Phase I-III clinical trials [27]. Previous studies showed that systemically administered hydroxyl-terminated PAMAM dendrimer (OH dendrimer) can selectively target TAMs in murine glioblastoma (glioma) models [28,29]. However, given the heterogeneous nature of TAMs, it is unclear what subset(s) are being targeted and what mechanism mediates the selective cell-targeting. In this study, we quantitatively examined the cell-level biodistribution kinetics after systemically administering OH dendrimers in two murine models of glioma. M-MDSCs can efficiently endocytose OH dendrimers in all reservoir tissues (bone marrow, spleen, peripheral blood, and tumor). In the tumor, M-MDSCs and microglia showed a high capacity of taking up OH dendrimers and these two cellular compartments accounted for more than half the amount of the OH dendrimer deposition in the tumor. The trafficking of M-MDSCs from bone marrow to the tumor region contributed to the tumor deposition of OH dendrimers. We also found the surface functionality of dendrimers significantly affected their ability to ‘target’ M-MDSCs. Finally, the unique serum proteins associated with each dendrimer surface functionality affected the dendrimer’s differential target to M-MDSCs.

2. Materials and methods

2.1. Generation of Cy5-labeled dendrimers

The G6 PAMAM hydroxyl (OH), amine (NH₂), and succinamic acid (SA) terminated dendrimers were purchased from (Dendritech, Inc). The NH₂ dendrimer was used for reaction after the evaporation of methanol from the stock solution. The OH and SA dendrimers were further functionalized with amine terminals to conjugate Cy5 mono NHS ester (Cytiva). For the Cy5-labeling of OH dendrimers: Step 1: Fmoc-GABA-OH (Sigma-Aldrich) was coupled with G6-OH using PyBOP (Merck) as a coupling reagent to produce an intermediate with protecting group Fmoc. Step 2: The Fmoc protecting group was removed using piperidine (Sigma-Aldrich) – DMF (Sigma-Aldrich) mixture to produce bi-functional dendrimers. The crude was purified by dialyzing (membrane cutoff = 12–14 kDa) against DMF (Sigma-Aldrich) for 24 h by changing the DMF every 8 h. Step 3: The conjugation of Cy5 mono NHS ester was carried out in the presence of borate buffer (pH 8.5) with pure bifunctional dendrimer to produce G6-OH-Cy5 conjugate. Similarly, amine surface G6 dendrimer was labeled with Cy5 using borate buffer (pH 8.5). For the Cy5-labeling of SA dendrimers, in step 1, G6 SA dendrimer was coupled with N-Fmoc 1,5-diaminobutane hydrobromide (Sigma-Aldrich) using EDC·HCl (Sigma-Aldrich) as a coupling reagent.

In step 2, the successful deprotection of Fmoc using piperidine (Sigma-Aldrich) DMF (Sigma-Aldrich) mixture resulted in bi-functional dendrimers. The Cy5-labeling of bi-functional dendrimers under DMSO (Sigma-Aldrich) and DIEA (Sigma-Aldrich) produced G6-SA-Cy5 conjugate in step 3. The synthesized G6 PAMAM-Cy5 conjugates are in good agreement with the reported literature data [30].

2.2. Cell lines

The GL261 glioma cells were cultured in RPMI (Invitrogen) with 1% penicillin-streptomycin (Invitrogen), 10% fetal bovine serum (FBS) (Thermo Scientific), and 4 mM L-Glutamine. KR158 glioma cells were maintained in Dulbecco modified Eagle medium (DMEM) supplemented with 10% heat-inactivated fetal bovine serum (FBS) and 1% penicillin-streptomycin. Cell cultured in wells were expanded in T75 flasks (Falcon) in a humidified incubator (Thermo Scientific) at 37 °C with 5% CO₂. All cell lines tested negative for mycoplasma based on DNA-based PCR tests.

2.3. M-MDSC induction and culture

Induction of M-MDSCs from bone marrow cells isolated from CCR2^{RFP/WT}/CX3CR1^{GFP/WT} transgenic mice or Wild Type (WT) C57BL/6 was adapted from previously published work [31]. Bone marrow cells collected from the femur were seeded at a density of 1×10^6 cells/mL in KR158 cell-conditioned culture media (50% v/v KR158 conditioned media + 50% RPMI-1640 (Gibco) + 10% FBS (Corning) + 1% penicillin-streptomycin (Corning), + 1% GlutaMax (Gibco) + 1% Non-Essential Amino Acids (Gibco), 0.22 μm sterile bottle-top filtered). Cells were cultured for 5 days. At the endpoint, suspension cells were collected from the supernatant and adherent cells by scraper (Fisher Scientific) after 15-min incubation at 37 °C, 5% CO₂ with enzyme-free cell dissociation buffer (Gibco). Flasks were twice-washed using 10–25 mL FACS buffer (10% FBS + 1× HBSS) and all cells were collected by centrifugation (500 ×g for 5 min at 4 °C). Cells were collectively resuspended in a 50 mL sterile conical (Falcon) in FACS buffer and counted using trypan blue exclusion method. Cells were then analyzed by flow cytometry.

2.4. Characterization of dendrimer size, size distribution, ζ-potential, and dendrimer-serum protein interaction

The physicochemical properties (size, size distribution, and ζ-potential) of NH₂, OH, and SA dendrimers were characterized using Lite-sizer 500 (Anton Paar Instruments) at 25 °C. To measure the hydrodynamic radius based on dynamic light scattering (DLS), all dendrimers with different terminal groups were dissolved in 1 × PBS buffer (pH = 7.4) at 1 mg/mL. The dendrimer solutions were filtered through a 0.22 μm 13 mm polyether sulfone (PES) syringe filter (Cytiva) before the size measurement within a 1 mL cuvette (Sarstedt). To measure the ζ-potential, dendrimers were diluted in 1 × PBS buffer (pH = 7.4) at 0.3 mg/mL. The dendrimer solutions were also filtered before the ζ-potential measurement within an omega cuvette (Anton Paar). To assess the interactions between dendrimers and serum proteins, dendrimers were incubated with mouse serum from C57BL/6 mice (in-house generated) for 30 min at 37 °C at a concentration of 0.86 mg/mL to allow the formation of the dendrimer-serum protein complex. The dendrimer-serum protein or the serum protein solutions were then diluted in 1 × PBS buffer (pH = 7.4) to reach a final concentration of 0.3 mg/mL before assessment.

2.5. Mice and *in vivo* tumor models

WT and transgenic CCR2^{RFP/WT}/CX3CR1^{GFP/WT} C57BL/6 mice were bred in-house at the UF animal facility. CCR2^{RFP/WT}/CX3CR1^{GFP/WT} transgenic mice was generated by cross-breeding CCR2 deficient mice (CCR2^{RFP/RFP}[B6.129(Cg)-CCR2^{tm2.1lfv}/JJ]) and CX3CR1 deficient mice

(CX3CR1^{GFP/GFP}[B6.129P-CX3CR1^{tm1Litt}/J]). All procedures involving animal housing, care, and surgical procedures were following the guidelines of the UF Institutional Animal Care and Use Committee.

To generate an orthotopic model of GL261 and KR158 murine gliomas, mice were anesthetized by controlled isoflurane inhalation, and their heads were shaved before intravenous analgesia administration. Surgical sites were prepared using 2–3 mm incisions at the midline of the skull. Stereotactic injection of 2 μ L at 1 μ L/min 5.0×10^4 cells suspended in methylcellulose was performed at 2 mm lateral from the bregma using a Hamilton syringe autonomously controlled by a micro-fluidic injection apparatus (Stoelting). Post-injection the dermal incision was closed *via* suture and bone wax application. Animals were placed on a cage warmer for post-surgical monitoring. For *in vivo* studies of dendrimer uptake and distribution, Mice received tail vein injections of SA and OH dendrimers (50 mg/kg) and NH₂ dendrimers (10 mg/kg). Cy5-labeled dendrimers were suspended in 100–200 μ L saline and filtered with 0.22 μ m 13 mm PES filters.

2.6. Flow cytometry sample preparation and analysis

Cells obtained from brain tumor, bone marrow (femur), spleen, and blood were analyzed by flow cytometry. Mouse blood was collected from the chest cavity post right atrium lancing using a 1 mL syringe coated with 0.5 M EDTA (Invitrogen). Approximately 200 μ L of blood was transferred to a 1.5 mL microcentrifuge tube (Fisher Scientific) containing 100 μ L 0.5 M EDTA (Invitrogen). Whole blood was centrifuged at 21 °C, 380 \times g for 5 min and the plasma was collected and stored at -80 °C in 1.5 mL microcentrifuge tubes. Before the collection of other organs, systemic perfusion was performed by needle insertion into the left ventricle and flushed with 20 mL 1 \times PBS (Gibco) using a 10 mL syringe (BD) and 25G butterfly infusion set (Exel). Brains were removed by sagittal and coronal partitioning of the skull using surgical scissors and transferred to a microscopy slide for tumor excision. To generate a single-cell suspension for analysis, tumor tissue was minced using a regular single-edge razor blade until a viscous suspension of cells was generated. Cells were then transferred to a 50 mL conical (Falcon) filled with Accumax dissociation buffer (Innovative Cell Technologies) and incubated in a 37 °C water bath for 5 min. Suspensions were then oscillated through a 1 mL single-channel pipet tip for 40 cycles and strained through a 40 μ m strainer into a 50 mL conical, followed by dilution with 5 mL FACS buffer (2 or 10% FBS, 1 \times HBSS or 1 \times PBS). Cells were collected by centrifugation at 380 \times g for 5 min at 4 °C, followed by resuspension in 70% v/v Percoll Solution (GE) (70% Percoll, 1% 1 \times PBS in RPMI-1640). Using a 5 mL syringe and 3-in. 18G needle, the 70% Percoll suspension of tumor cells was injected below a layer of 37% v/v Percoll (4 mL, 37% Percoll, and 1% 1 \times PBS in Phenol-free RPMI-1640) (Gibco) in a 15 mL conical. Samples were subsequently centrifuged at 500 \times g for 30 min at 21 °C (level 1 acceleration, level 0 deceleration). The resulting tumor cell interface between Percoll layers was removed (1 mL) by a single channel pipet and transferred to a 1.5 mL microcentrifuge tube. Cells were centrifuged at 500 \times g for 5 min at 4 °C and washed and resuspended with ice-cold FACS Buffer (2% or 10% FBS in 1 \times HBSS (Gibco) or 1 \times PBS). Femurs were harvested and ends clipped with dissecting scissors after connective tissues were removed. The isolated femurs were placed in 0.5 mL microcentrifuge tubes with an 18G needle pierced bottom, cap removed, and tube nested within a secondary 1.5 microcentrifuge tube containing 100 μ L ice cold ACK lysis buffer (Gibco). Microcentrifuge tubes with femurs were centrifuged at 5700 RPM for 20 s at 21 °C to capture bone marrow. Spleens were excised and transferred to a petri dish on ice for mincing using a regular single-edge razor blade (Personna) after injection with 1 mL of ice-cold 1 \times HBSS (Gibco) or 1 \times PBS using a 3-in. 18G needle (Air-Tite) and 5 mL syringe (BD). Dispersed tissues were aspirated into a 5 mL syringe *via* a 3-in. 18G needle and transferred to a 15 mL conical. Around 5 mL of ice-cold 1 \times HBSS or 1 \times PBS was added, and cells were mechanically dissociated by the oscillation of the volume through the

syringe and needle for 20 cycles. The resulting splenocyte suspension was centrifuged at 380 \times g for 5 min at 4 °C. 1 mL ice cold ACK Lysis Buffer (Gibco) was added to bone marrow cells, leukocytes, and splenocyte to resuspend post centrifugation for 5 min and subsequently diluted with 5 mL ice-cold FACS Buffer (2 or 10% FBS in 1 \times HBSS (Gibco) or 1 \times PBS) then strained through a 40 μ m cell strainer (Fisherbrand). Cells from each tissue were isolated by centrifugation at 380 \times g for 5 min at 4 °C. To remove all visibly present red blood cells, leukocytes were repeatedly cycled, up to four additional times, through ACK lysis buffer (Gibco) and FACS buffer wash as previously described. Viability was manually determined by cell count using a standard trypan blue (Corning) exclusion method.

Single-cell suspensions were prepared as described in the above sections. Samples were stained with viability dye (Violet, Invitrogen) in 1 \times PBS pH 7.4 (Gibco) at RT protected from light for 15 min. Cells were resuspended and washed with FACS buffer (2 or 10% FBS, 1 \times HBSS or 1 \times PBS) and stored on ice until analysis. Samples were analyzed *via* a single flow cytometry tube on a Sony Spectral Analyzer (SP6800). A multi-color reference control panel consisting of transgenic single color CCR2^{RFP/WT} and CX3CR1^{GFP/WT} bone marrow cells, viability dye–violet (Thermo Scientific), and Cy5-positive WT C57BL/6 bone marrow cell suspensions was utilized to unmix panels as appropriate. Raw data was subsequently analyzed and graphically illustrated using FlowJo software (BD Biosciences).

2.7. In vitro dendrimer uptake study

Transgenic CCR2^{RFP/WT}/CX3CR1^{GFP/WT} or WT C57BL/6 bone marrow cells were derived into M-MDSCs *ex vivo* as described herein (CCR2^{RFP+}/CX3CR1^{GFP+}). Cells were washed with FACS buffer (10% FBS, 1 \times HBSS) and resuspended in serum-free 1 \times HBSS (Gibco). Viability and concentration were determined by trypan blue exclusion. Cells were adjusted to a concentration of $\sim 1 \times 10^6$ /mL in 1.5 mL microcentrifuge tubes (Fisher Scientific) and centrifuged at 500 \times g for 5 min at 4 °C. Cells were resuspended in 400 μ L of dissolved dendrimer solution at a concentration range from 1 to 100 μ g/mL in 1 \times HBSS or 1 \times PBS at room temperature and incubated for 30 min protected from light. Samples were then washed in 1 \times HBSS, stained for viability, and resuspended with FACS buffer in three technical repeats and analyzed *via* Spectral Flow Cytometry as described herein. To determine how dendrimer-associated serum proteins affect their interaction with M-MDSCs *in vitro*, dendrimer stock solutions were prepared by fully solubilizing dendrimers in 1 \times PBS pH 7.4 (Gibco), followed with filtration through a 13 mm 0.22 μ m PES syringe filter (Cytiva). Solutions were diluted at room temperature to concentration of 0.86 mg/mL in either competent or heat-inactivated (60 °C for 30 min) sex pooled, complement preserved, C57BL/6 murine serum (Charles River) in 1.5 mL microcentrifuge tubes. Dendrimer-serum stock solutions were then incubated at 37 °C for 30 min and brought to room temperature before co-incubation with cells at escalating doses (5–100 μ g/mL) in three biological repeats. The dendrimer uptake as indicated by Median Fluorescence Intensity (MFI) was subjected to flow cytometry analysis by gating out the CCR2^{RFP+}/CX3CR1^{GFP+} (M-MDSC) or WT equivalent population.

2.8. Immunofluorescence study

To determine the biodistribution and the cell uptake of dendrimers, Cy5-labeled dendrimers were injected *via* tail vein into transgenic CCR2^{RFP/WT}/CX3CR1^{GFP/WT} or wildtype C57BL/6 mice at tolerable doses (50 mg/kg for SA, OH dendrimers and 10 mg/kg for NH₂ dendrimers). Euthanized animals were systemically perfused with 20 mL 1 \times PBS (Gibco) and 20 mL 4% w/v paraformaldehyde (PFA) buffered solution. (Thermo Scientific) using a 50 mL syringe and 25G butterfly needle infusion set. Brain (tumors), spleens, and femurs were excised, and connective tissues were removed prior to transfer to 5 mL of 4% w/v

PFA at 4 °C for 1 h (brains and spleens) or 72 h (femurs) at 2–8 °C. Brains (tumors) and spleens were then transferred to a 30% w/v sucrose (Fisher Scientific) in water (Corning) solution for ≥ 24 h in 15 mL conical tubes stored at 2–8 °C. Femurs were subsequently transferred to 5 mL of decalcification solution (20% EDTA, 10 N NaOH, pH 7.4) for 4 days at 2–8 °C and then a 30% w/v sucrose solution for 24 h at 2–8 °C. All tissues were embedded in optimal cutting temperature compound (Fisher Scientific) and cryo-sectioned at 10 μ m or 30 μ m thick sections at –25 °C. Sections were prepared by addition to microscopy slides (Fisher Scientific), washed for 3 repetitive cycles with cold 1 \times Dulbecco's Phosphate Buffered Saline (DPBS) in a staining dish. For vascular endothelial cell staining of brain tissues, an anti-mouse CD31-Spark YG 570 labeled mAb (BioLegend) was added to hydrophobic pen (Vector Laboratories) encircled sections at a concentration of 10 μ g/mL. Slides were then mounted with Vectashield anti-fade mounting medium with DAPI stain (Vector Laboratories) and coverslip. Slides were sealed with CoverGrip sealant and subsequently stored at 2–8 °C protected from light in the staining tray. Sections were analyzed at high magnification using an inverted Nikon A1R confocal microscope. Widefield fluorescent images were generated using a Keyence BZ-X800 or Nikon Ti-E for fluorescence microscopy. Widefield fluorescence microscopy images were processed using Nikon Elements software v5.21 and confocal fluorescence microscopy using Fiji v2.9.0.

2.9. Quantification of dendrimer concentration in plasma

Blood was collected from CCR2^{RFP/WT}/CX3CR1^{GFP/WT} mice bearing 3–4-week KR158 or GL261 gliomas at 24- or 72-h post-dendrimer administration (tail vein) as previously described herein. Plasma samples were thawed from –80 °C storage to room temperature and diluted 1:4 with 1 \times PBS (Gibco). Samples were then transferred to a 96-well clear bottom black plate (Thermo Scientific) and analyzed for absolute fluorescence intensity from Cy5 (635/675 (ex/em), integration: 400 ms, read height: 3.0 mm) using a Molecular Devices SpectraMax iD3 Multi-Mode Microplate Reader. Samples were plotted against a standard curve of Cy5 in murine serum and interpolated post-transgenic murine plasma background subtraction. The percentage of the injected dose was calculated by dilution factors \times estimated dendrimer concentration \times plasma volume (estimated to be 1.8 mL/mouse) / total injected dose. Samples were evaluated by 3 technical repeats.

2.10. Data reporting and statistical analysis

Each *in vitro* assay was performed using a minimum of three technical repeats and three biological repeats. All data was processed and graphed using GraphPad Prism v10.1.1 displaying average, standard deviations, error, and statistical *p*-values by one or two-way ANOVA as appropriate per data set. Each *in vivo* assay was performed using a minimum of $n = 6$ mice based on the median of a group comparison using a one- or two-way ANOVA between the calculated min and max degrees of freedom ((DF = $k(n-1)$ n = sample size, k = number of groups). Representative immunohistochemistry $n = 1$ (IHC) and microscopy tissue samples were displayed.

3. Results and discussion

3.1. M-MDSCs represent a significant population in the glioma TME

To determine how dendrimers interact with M-MDSCs and other immune cells *in vivo*, we first characterized the profiles of M-MDSCs and other infiltrative immune cells in a GL261 mouse glioma model. This model well-recapitulates the histology of glioma and has been extensively used to test the therapeutic responses in the literatures [32]. GL261 gliomas were established in CCR2^{RFP/WT}/CX3CR1^{GFP/WT} transgenic mice, which allows the direct surveillance of the profile of infiltrative immune cells *via* the endogenously expressed red fluorescent

protein (RFP) for chemokine receptor two (CCR2) and green fluorescent protein (GFP) for CX3C motif chemokine receptor 1 (CX3CR1) [20,33]. When expressed jointly, these G-Protein Coupled Receptors (GPCRs) have been established as an equivalent biomarker for the M-MDSC cell subset, as defined by CD45⁺Ly6G⁺Ly6C⁺CD11b⁺ populations [2]. Moreover, bone marrow-derived CCR2⁺/CX3CR1⁺ M-MDSCs suppress both CD4⁺ and CD8⁺ T cells [31]. At 2–3 weeks after the tumor initiation, we performed the flow cytometry analysis of the M-MDSC population from bone marrow, blood, and spleen. Our results showed that M-MDSCs accounted for $11.4 \pm 0.4\%$ and $3.8 \pm 0.1\%$ of total cells in the bone marrow and spleen of GL261 tumor-bearing mice (Fig. 1A and B, orange). CCR2 and its cognate receptors mediated M-MDSCs egress from bone marrow into peripheral blood [31], in which the M-MDSCs comprised $8.5 \pm 1.5\%$ of the blood leukocytes (Fig. 1A and B, orange); M-MDSCs infiltrated the glioma through peripheral blood, ultimately comprising $22.1 \pm 1.0\%$ of the stromal cells in the GL261 tumor (Fig. 1C, orange). In the TME, M-MDSCs were shown as the RFP and GFP co-localized cells, as indicated by the arrows in Fig. 1D. The CCR2^{RFP/WT}/CX3CR1^{GFP/WT} transgenic mice also enabled us to profile other immune cell subsets in the glioma TME. Based on previously published data [20], the CCR2⁺/CX3CR1⁺ subsets ($16.7 \pm 3.0\%$, Fig. 1C, dark green, abbreviated as microglia) were CD45^{low}/MHC⁺/F4/80⁺/CD11c[–]/CD11b^{medium}, likely representing the CNS tissue-resident microglia; the CCR2⁺/CX3CR1[–] subsets ($4.4 \pm 2.0\%$, Fig. 1C, red, abbreviated as CCR2⁺) were CD45⁺/MHCII⁺/F4/80[–]/CD11c[–]/CD11b^{low}, likely representing another myeloid cell that originated outside of the CNS; the CCR2[–]/CX3CR1[–] subsets ($26.4 \pm 4.9\%$, Fig. 1C, grey, abbreviated as other cells) were a collection of tumor cells and other tumor stroma cells. Finally, the CCR2[–]/CX3CR1^{int} subsets accounted for $30.5 \pm 5.9\%$ of tumor stromal cells (Fig. 1C, light green, abbreviated as CXCR1^{int}). Given these cells were a mixed population of CD45^{low} and CD45^{high} [20], it is possible that they infiltrated the glioma from outside of the brain.

3.2. Tumor M-MDSCs show a high capacity for dendrimer uptake

Previous studies have established that, in the presence of neuro-inflammation/tumor lesions, systemically injected OH dendrimers can selectively localize in activated glial cells in a spectrum of central nervous system (CNS) disorders [28–30]. We first evaluated OH dendrimer (Generation 6) as a model dendrimer to probe the dendrimer uptake capacity of different cell subsets within the glioma TME, the lymphoid organs (bone marrow, spleen), and the blood. Mice with established GL261 gliomas were injected systemically with OH dendrimers at 50 mg/kg – a dose that has been well-tolerated *in vivo* [34]. To track the dendrimer–cell interaction, we fluorescently labeled the OH dendrimer with a minimal amount of Cy5 dye (~1% or 5% by wt%) [29]. At 24 h after injection, different cell subsets within the stroma of the GL261 tumor were isolated and subsequently subjected to flow cytometry analyses to determine the Cy5 Median Fluorescence Intensity (MFI) within each cell subset, which indicates the amount of dendrimer being endocytosed by the cells. Remarkably, tumor M-MDSCs and microglia showed a capacity for high dendrimer uptake (Fig. 2A). Specifically, the MFI of tumor M-MDSCs = 1061 ± 535 , which was significantly higher than CX3CR1^{int}, CCR2⁺, and other cells (Fig. 2B). This indicated that tumor M-MDSCs have a higher capacity for endocytosing OH dendrimers than other cell subsets within the GL261 tumor. We next evaluated the composition of all dendrimer-positive cells within the GL261 tumor by gating out the dendrimer-positive populations from the whole tumor stroma cells. The composition of the dendrimer-positive populations was then analyzed based on the CCR2 (RFP) and CX3CR1 (GFP) expression (Fig. 2C). Our results showed that the majority of the dendrimer-positive cells were mostly distributed within 4 cellular compartments, *i.e.*, M-MDSC ($19.7 \pm 6.7\%$), microglia ($25.1 \pm 3.4\%$), CX3CR1^{int} ($28.6 \pm 6.9\%$), and other cells ($24.0 \pm 6.2\%$) (Fig. 2D). The CCR2⁺ compartment only accounted for $2.7 \pm 0.7\%$ of dendrimer-

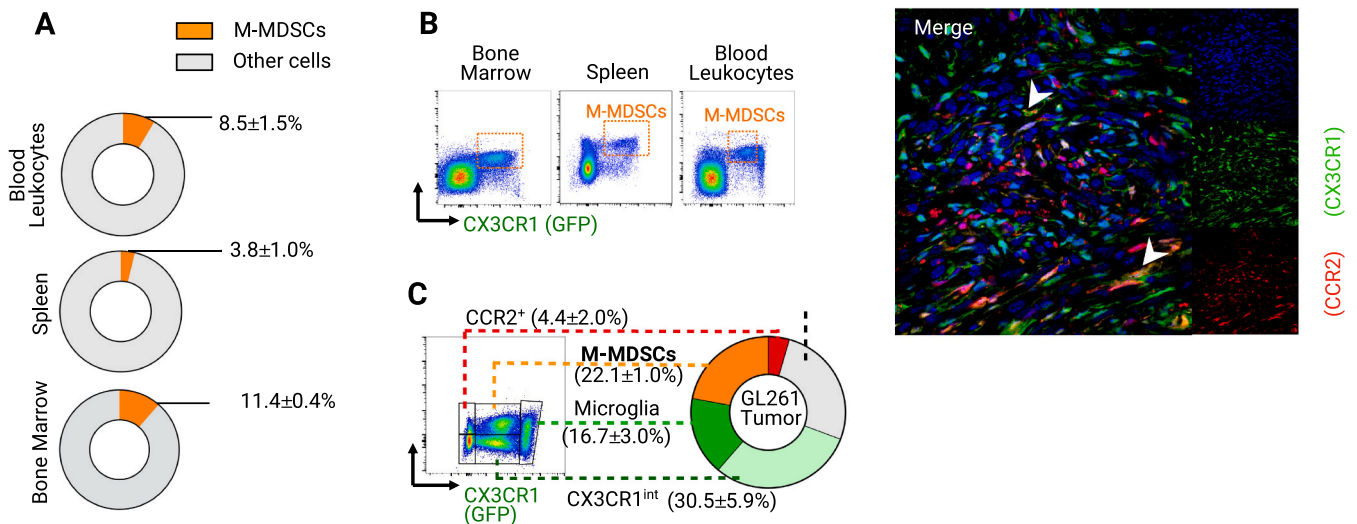


Fig. 1. The $CCR2^{RFP/WT}CX3CR1^{GFP/WT}$ transgenic mice enable direct surveillance of M-MDSCs in mouse glioma model. **A)** in mice with established GL261 tumors, the pie graph shows the flow cytometry measurement of the average percentage of M-MDSCs reside in their reservoir tissues such as bone marrow, spleen, and peripheral blood leukocytes. At 3–4 weeks after tumor initiation, tissues from 6 tumor-bearing mice were analyzed. **B)** Gating strategy for the M-MDSCs cells in each tissue: the M-MDSCs are defined as the $CCR2^+/CX3CR1^+$ population, which is indicated in the orange box. **C)** Gating strategy and the average percentage of major cell subsets in the GL261 tumor stroma. $CCR2^+/CX3CR1^+$ cells (orange): M-MDSCs; $CCR2^-/CX3CR1^+$ cells (dark green): likely representing the CNS tissue-resident microglia; $CCR2^-/CX3CR1^{mcdidum}$ cells (light green): $CX3CR1^{int}$, likely represent immune cells infiltrate brain tumor from external sources; $CCR2^+/CX3CR1^-$ cells (red): $CCR2^+$, likely represent other infiltrate myeloid cells originated outside of the CNS. $CCR2^-/CX3CR1^-$ cells (grey): other cells, a collection of tumor cells and other tumor stroma cells. At 3–4 weeks after tumor initiation, tissues from 6 tumor-bearing mice were analyzed. **D)** confocal microscopy image of tumor (KR158). Arrow indicates the $CCR2^+/CX3CR1^+$ M-MDSCs. Red: RFP/CCR2; Green: GFP/CX3CR1; Blue: DAPI. (For interpretation of the references to color in this figure legend, the reader is referred to the web version of this article.)

positive cells (Fig. 2D), potentially due to their small numbers within the tumor stroma (~5%, Fig. 1C).

While the GL261 glioma model recapitulates the histology of glioma [32], it is well-established that the GL261 glioma model, unlike human glioblastoma, is immunogenic [32,35,36]. Specifically, GL261 has high MHC-I expression and a high tumor mutational load [35] and responds well to checkpoint inhibitors [36]. We next sought to characterize the dendrimer interactions with M-MDSC and other immune infiltrative cells in an KR158 model, which has lower populations of infiltrative M-MDSC and is resistant to checkpoint inhibitors [37,38]. Interestingly, when comparing the overall Cy5 MFI of all tumor stromal cells, the GL261 tumor showed 1.6-fold higher MFI (mean = 946.8) than the KR158 model (mean = 598.2), indicating a higher dendrimer deposition in the GL261 tumors as compared to the KR158 tumors (Fig. 2E). The different dendrimer deposition between the two glioma models was also reflected at the cellular level. The cell subsets within the GL261 tumor showed approximately 2–3-fold higher dendrimer uptake than the KR158 tumor (Fig. 2F). Surprisingly, when comparing the cellular composition of dendrimer-positive populations, around $53.4 \pm 6.0\%$ of dendrimer-positive cells in the KR158 tumor were located in the microglia compartment, while only $6.4 \pm 0.8\%$ and $12.1 \pm 2.6\%$ of dendrimer-positive cells were located in the M-MDSC and $CX3CR1^{int}$ compartments respectively (Fig. 2G). Although the KR158 tumor had lower dendrimer deposition and different compositions of dendrimer-positive cells compared to the GL261 tumor, the M-MDSCs and microglia in both tumor models showed higher dendrimer uptake than other cell subsets (Fig. 2F, Fig. S1A–C). In summary, our data based on two different glioma models indicated that the monocytic myeloid cells largely contributed to the tumor depositions of OH dendrimers. We next sought to evaluate whether the percentage of each cell subset within the tumor correlated with the amount of dendrimer deposition in both tumor models. Analyses of the Pearson correlation coefficients showed that the percentage of tumor-infiltrative cells (M-MDSCs, Microglia, $CX3CR1^{int}$, and $CCR2^+$) generally had positive correlations with the amount of OH dendrimer depositions in both tumor models (Fig. 2H).

Specifically, M-MDSCs and $CX3CR1^{int}$ population showed better correlation ($r > 0.2$ or $r > 0.6$) than other cell subsets in both tumor models. However, the percentage of $CCR2^-/CX3CR1^-$ subsets (other cells), which are a collection of tumor cells and other tumor stroma cells, showed a strong negative correlation with OH dendrimer deposition ($r < 0.6$).

The selective uptake of OH dendrimer by tumor-associated microglia/macrophages has been reported in previous studies [28,29]. However, ontogeny differences between CNS-resident microglia and bone marrow-derived macrophages suggests distinct functions in brain cancer and different responses to macrophage-targeting therapeutics [39,40], which highlights the importance of analyzing the cell-level biodistribution of nanotherapeutics. Both the M-MDSCs originated from bone marrow and the CNS-resident microglia showed a strong capacity for taking up OH dendrimers in our study. However, it is possible these cell subsets endocytose dendrimers through different mechanisms. For example, bone marrow-derived M-MDSCs and tumor-associated macrophages are more associated with phagocytosis and antigen-presentation. They are present at a higher density in the perivascular niche than microglia, which display signatures associated with synaptic pruning [41,42]. We also noticed the differential dendrimer deposition between the GL261 and KR158 tumors. This difference might be associated with the different immunogenicity of GL261 and KR158 tumors [32]. The immunogenic GL261 tumor has a ‘hotter’ tumor milieu with more infiltrative immune cells than KR158 tumors [32]. Since ours and other studies showed infiltrative myeloid cells within the tumor often contribute to the tumor-accumulation of nanoparticles [43,44], it is possible that the higher OH dendrimer deposition in the GL261 tumor was associated with the higher amount of infiltrative immune cells in this model. The KR158 tumor showed an ectopic growth on the surface of the cerebral cortex, while the GL261 histology was more representative of the human glioma (Fig. S2). As the tumor pathophysiology can also significantly impact nanoparticle deposition [45], it remains to be determined whether the histological difference could also contribute to the differential dendrimer uptake.

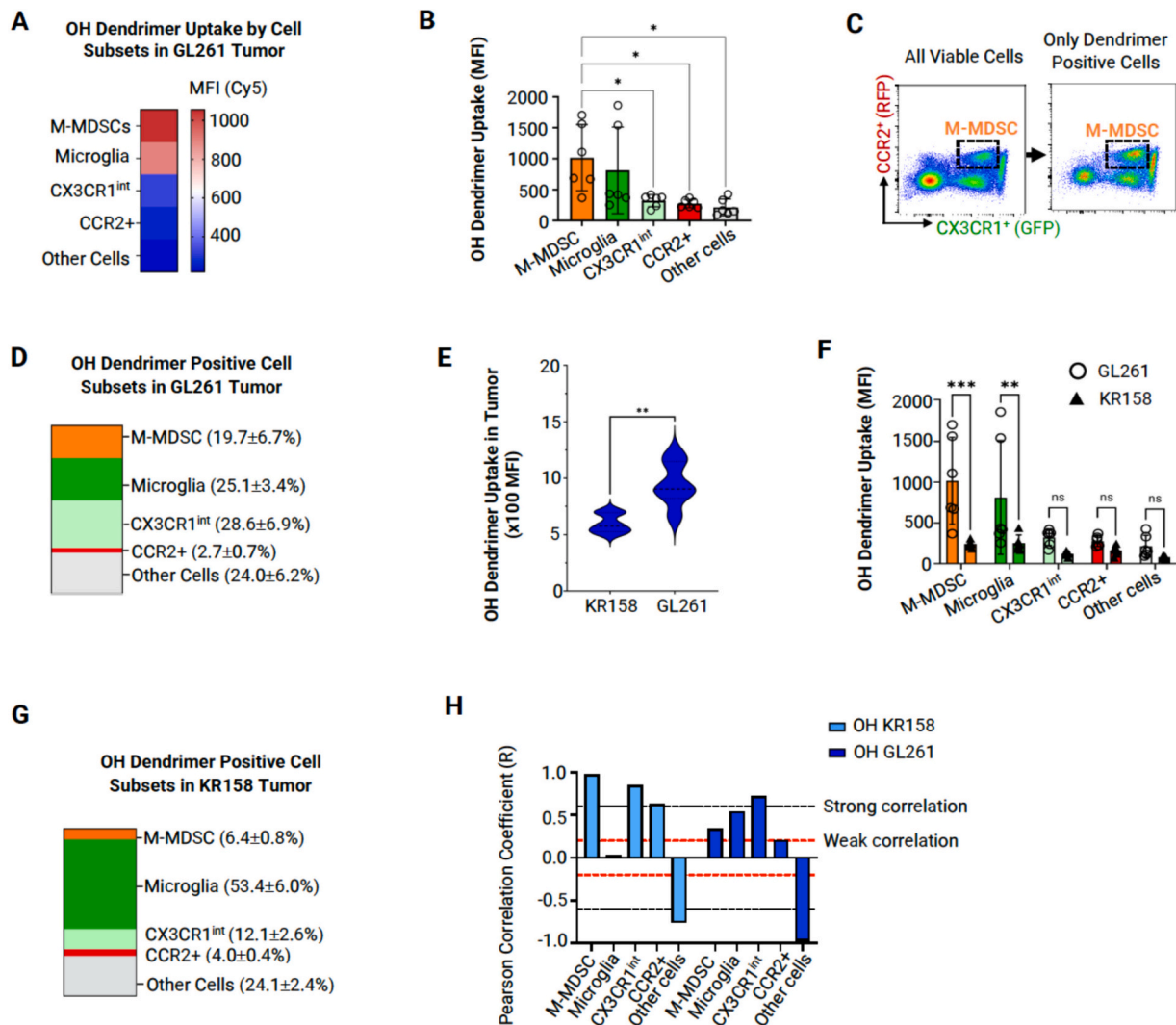


Fig. 2. Tumor M-MDSCs efficiently endocytose dendrimers with high capacity.

Cy5-labeled OH dendrimers (50 mg/kg) were systemically injected into GL261 and KR158 tumor bearing transgenic mice (CCR2^{WT/RFP}CX3CR1^{WT/GFP}) at 3–4 weeks post-implantation; at 24 h post injection, OH dendrimers uptake in myeloid subsets (indicated by Cy5 Median Fluorescence Intensity (MFI)) and the composition of dendrimer-positive cells (indicated by percentage of dendrimer-positive subset) within the tumor were analyzed through flow cytometry. **A**) The capacity of each cell subsets to uptake OH dendrimers within the GL261 gliomas at 24 h post-injection. This is indicated by the MFI, which representatively measures the median number of dendrimers deposited per single cell. **B**) The statistical analysis of **A**). **C**) Representative density plot of GL261 tumor stromal cells (left panel) and in the same tumor, the density plot of OH dendrimer-positive cells (right panel). M-MDSCs are shown in the box. **D**) Statistical analysis of the density plot of dendrimer-positive cells in **C**) (right panel), which shows the composition of dendrimer-positive cells in each cellular compartment within the GL261 tumor as a percent of a whole ($n = 6$). **E**) Comparison of the mean, upper and lower quartiles of OH dendrimer deposition in tumor as measured by MFI between GL261 and KR158 gliomas. **F**) Comparison of OH dendrimer uptake capacity (MFI) in each cell subsets between GL261 and KR158 tumors. **G**) Composition of dendrimer-positive cells in each cellular compartment within the KR158 tumor as a percent of a whole ($n = 6$). **H**) the correlation analysis between the abundance of cell subset (indicated by the percentage of cell subset within all tumor stroma cells) and the dendrimer deposition within the tumor (indicated by Cy5 MFI of all tumor cells) for both GL261 and KR158 tumors. The Pearson correlation coefficient (R) is based on 95% confidence interval. Weak correlation, $R > 0.2$ or $R < -0.2$; strong correlation, $R > 0.6$ or $R < -0.6$. For all *in vivo* experiment, data were generated based on 6 mice of both male and female sexes, * $p < 0.05$, ** $p < 0.01$, *** $p < 0.001$, ns = not statistically significant.

3.3. The trafficking kinetics of M-MDSC contribute to the dendrimer accumulation in the tumor

In the presence of tumor lesions, the production of M-MDSCs was accelerated in the bone marrow, from which these cells are directly recruited to the brain tumor through peripheral blood or indirectly from the spleen, which serves as the temporary reservoir of M-MDSCs [20,31,33] (Fig. 3A). To determine whether the trafficking kinetics of M-MDSCs affected the deposition of dendrimer in the brain tumor, we first quantified the cellular uptake of OH dendrimers (MFI) by M-MDSCs located in bone marrow, spleen, peripheral blood, and tumor (GL261) at 24 h after dendrimer injection (50 mg/kg). Dendrimer uptake was observed in the M-MDSCs from all tissues analyzed (Fig. 3B). In the

femur bone, OH dendrimers were mostly distributed in the red marrow, where hematopoiesis led to the product of leukocytes (Fig. S3A). In the spleen, OH dendrimers were mostly distributed in the red pulp (Fig. S3B), where MDSCs are located [46]. The blood M-MDSCs showed the highest dendrimer uptake (MFI = 1371 ± 494), probably because blood M-MDSCs can directly access the dendrimers in the circulation without the limitation of any tissue barriers. We further analyzed the dendrimer uptake in different blood leukocytes (identified through the FSC- and SCC-based scattered plots). The dendrimer uptake was highest in granulocytes (MFI = 1112 ± 232), followed by monocytes (MFI = 231.7 ± 48) and lymphocytes (MFI = 172.8 ± 56) (Fig. 3C and Fig. S4A). Approximately 95% of granulocytes showed dendrimer uptake, compared to ~40% for monocytes and ~30% for lymphocytes

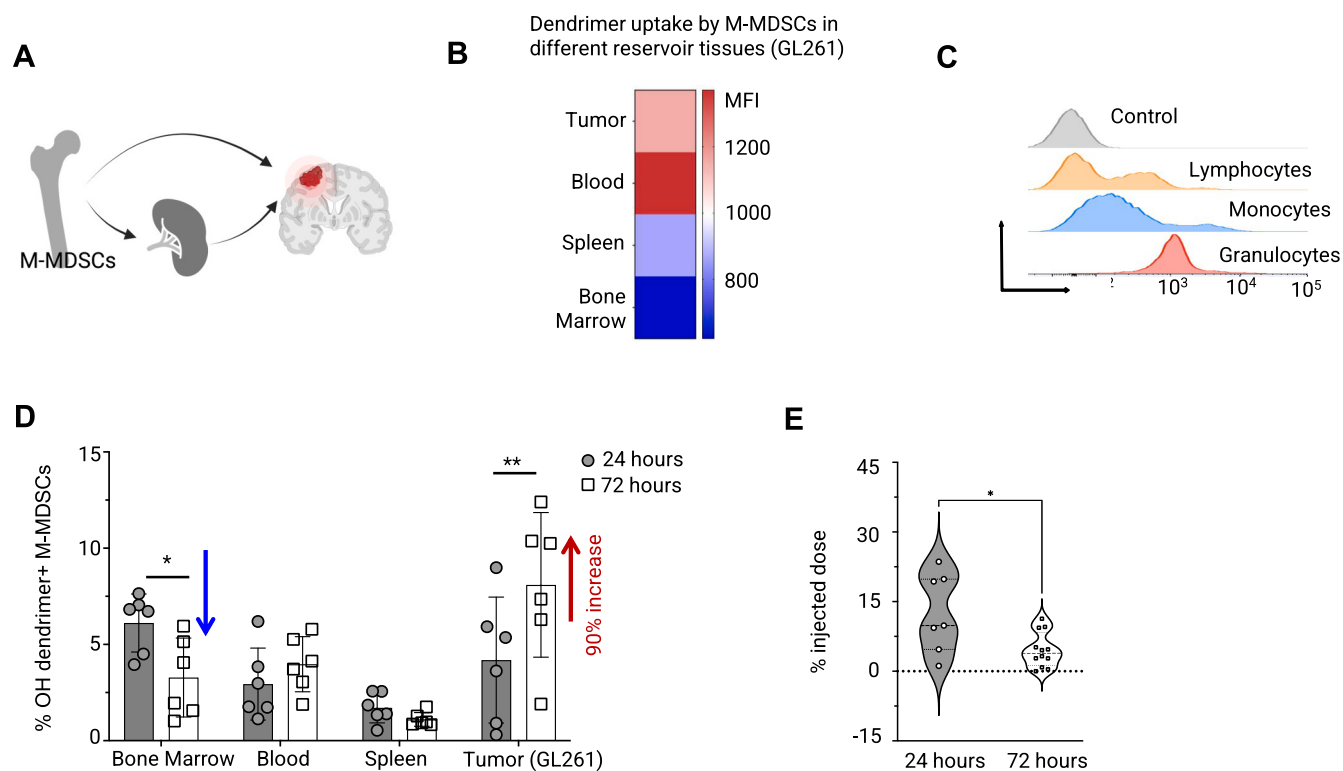


Fig. 3. The trafficking kinetics of M-MDSC contributes to the dendrimer accumulation in the tumor. **A)** Graphical illustration shows the trafficking kinetics of M-MDSCs. M-MDSCs are recruited to the brain tumor from bone marrow (hematopoietic tissue) or spleen (temporary reservoir) through systemic circulation (blood). **B)** Heatmap shows the OH dendrimer uptake capacity (indicated by Cy5 MFI) for M-MDSCs in bone marrow, spleen, blood, and tumor in GL261 glioma bearing mice (average MFI from 6 mice). **C)** Histogram shows the overall OH dendrimer uptake capacity (indicated by Cy5 MFI) for white blood cells isolated from the peripheral blood of GL261 tumor-bearing mice. Control cells (no dendrimer injection). Cell subsets (lymphocytes, monocytes, granulocytes) were gated based on the scattered plot FSC vs. SSC. **D)** Comparison of the percentage of dendrimer-positive M-MDSCs between 24 h vs. 72 h after dendrimer injection. Data was obtained from GL261 tumor-bearing mice. **E)** Quantification of OH dendrimer concentrations in the plasma of GL261 tumor-bearing C57BL/6 mice at 24 h ($n = 7$) and 72 h ($n = 12$) post-dendrimer injection. For all other experiments in this figure, flow cytometry analyses were based on 6 GL261 tumor-bearing mice that received systemic injection of 50 mg/kg OH dendrimers. * $p < 0.05$, ** $p < 0.01$.

(Fig. S4B). Since M-MDSCs are constantly being recruited to the tumor in large amounts during tumor development, we hypothesize that blood M-MDSCs may carry endocytosed dendrimer to the tumor while they infiltrate the tumor stroma. To test this hypothesis, we analyzed the change of the dendrimer-positive M-MDSCs percentage between the 24- and 72-h window in two cohorts of mice. In bone marrow, we observed a 50% decrease in the percentage of dendrimer-positive M-MDSCs within the 48-h window (Fig. 3D). This decrease in dendrimer-positive M-MDSCs could be caused by two factors. First, the emergency myelopoiesis in cancer leads to the accelerated generation of new M-MDSCs, which could dilute the dendrimer-positive populations; Second, the initial dendrimer-positive M-MDSCs could egress from the bone marrow, further diluting the percentage of dendrimer-positive M-MDSC in the bone marrow. In the GL261 tumor, we observed a 90% increase in the percentage of dendrimer-positive M-MDSCs (Fig. 3D) but not the tissue-resident microglia (Fig. S4C). This significant increase in dendrimer-positive M-MDSCs may have resulted from the recruitment of external dendrimer-positive M-MDSCs to the tumor milieu during the 48-h window. It is less likely that tumor M-MDSCs could uptake more dendrimers within the 48–72 h window, as we did not observe a significant increase of percentage of dendrimer-positive microglia between the 24 and the 72 h (Fig. S4C). Further analysis of serum concentration showed that the amount of OH dendrimers decreased from $12.5 \pm 8.5\%$ (total injected dose) at 24 h to only $4.6 \pm 3.7\%$ at 72 h (Fig. 3E). This significant decrease of dendrimer plasma concentration also correlated with the ~ 5 -fold decrease of dendrimer concentration in the brain tumor,

which was reported in a previous study based on the same tumor model and dendrimer generation [28]. There was no significant change in dendrimer-positive populations in the blood and spleen M-MDSCs. Collectively, this evidence suggests that the recruitment M-MDSCs could contribute to the tumor accumulation of dendrimers.

For decades, the Enhanced Permeability and Retention (EPR) effect has been used as the guiding principle for designing tumor-targeting nanomedicine [2]. Previous studies based on this theory showed that the accumulation of OH dendrimers in glioma was largely attributed to their neutral surface and ultra-small sizes (sub-10 nm), which allowed them to efficiently cross the impaired blood-brain tumor barriers (BBTB) taken up by myeloid cells within the tumor through EPR effect and [28,29]. However, it was not clear whether other complementary mechanism(s) could also contribute to the dendrimer accumulation in the tumor. Historic studies demonstrated myeloid cells can modulate the pharmacokinetics, biodistribution, and efficacy of nanotherapeutics [12,13]. Recent studies argued that circulating myeloid cells, such as inflammation-associated monocytes and granulocytes can actively transport nanoparticles from the blood to the tissue when they infiltrate the inflamed tissue [14,43,47]. By showing that highly tumor-infiltrative M-MDSCs can contribute to the tumor accumulation of OH dendrimers, our study confirmed that, in addition to the EPR effect, the cell-mediated transport served as a complementary mechanism for tumor accumulation of dendrimers in a mouse model of glioma. Although the results showed that the granulocytes in the blood also had large amount of dendrimer uptake, this study and a prior one, based on

the same glioma models, did not observe the presence of Ly6G⁺ granulocytes in the glioma tumor milieu [20]. For this reason, we think that granulocytes did not contribute to the dendrimer deposition in the glioma. This phenomenon can be leveraged to design M-MDSC-targeting therapeutics for enhanced tumor delivery. Future studies in this direction could benefit from a quantitative study of the tumor accumulation

of adoptively transferred dendrimer-positive M-MDSCs.

3.4. Dendrimer surface functionality affects their interactions with M-MDSC *in vivo*

Dendrimer surface functionality can significantly affect their *in vivo*

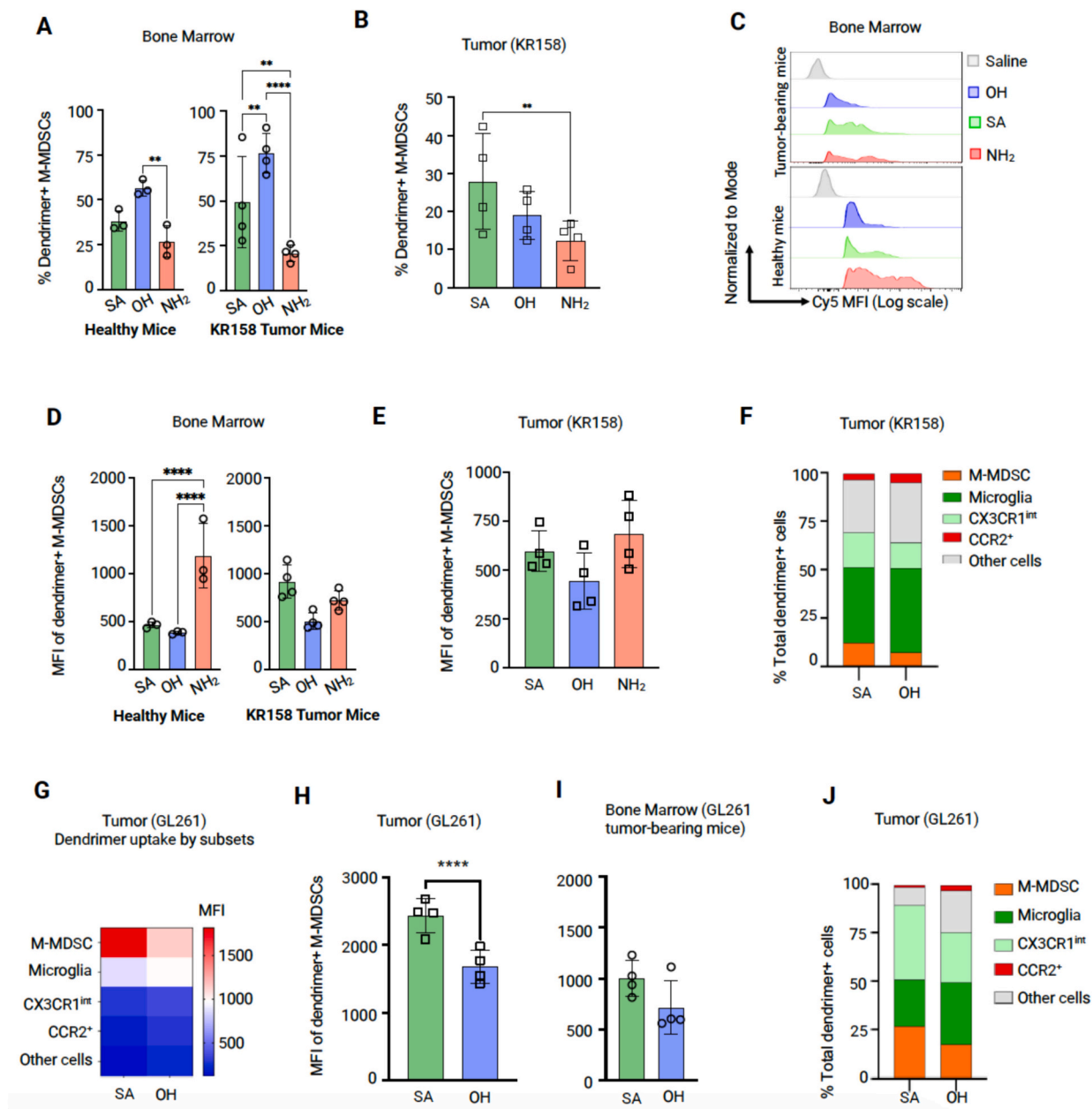


Fig. 4. Dendrimer surface chemistry affects their interactions with M-MDSC *in vivo*. To determine how dendrimer surface chemistry affect their interaction with M-MDSCs *in vivo*, dendrimers with different terminal groups (i.e. Succinamic acid: SA, hydroxyl: OH, and amine: NH₂) were systemically injected into healthy ($n = 3$) or tumor bearing mice ($n = 4$) at tolerable doses (50 mg/kg for SA and OH, 10 mg/kg for NH₂). At 24 hours after dendrimer injection, the bone marrow and tumor were isolated for flow cytometry analysis. **A**) comparison of the percentage of dendrimer-positive M-MDSCs (% dendrimer+ M-MDSCs) in the bone marrow of healthy (left) and KR158 tumor-bearing mice (right) between SA, OH, and NH₂ dendrimers. The % dendrimer+ M-MDSCs measure dendrimer's ability to 'target' M-MDSCs in the tissue. **B**) comparison of the percentage of dendrimer-positive M-MDSCs in the KR158 tumor between SA, OH, and NH₂ dendrimers. **C**) Representative histograms comparing the Cy5 MFI of dendrimer-positive cells in the bone marrow of KR158 tumor-bearing mice (top) and healthy mice (bottom) respectively. **D, E**) Comparison of the M-MDSC's capacity to endocytose SA, OH, and NH₂ dendrimers (indicated by MFI). Plot shows M-MDSCs isolated from **D**) the bone marrow of healthy mice (left) and KR158 tumor bearing mice (right) and **E**) the KR158 tumors. **F**). Comparison of SA and OH dendrimers for the composition of dendrimer-positive cells within the KR158 tumor. **G**) the heatmap shows the uptake capacity of SA and OH dendrimers (indicated by Cy5 MFI) by different cell subsets within the GL261 tumor. Data displayed is median. **H, I**) Statistical analysis comparing the SA and OH dendrimers in terms of their uptake capacity (indicated by Cy5 MFI of dendrimer-positive cells) by M-MDSCs within the tumor (**H**) and bone marrow (**I**) of the GL261 tumor bearing mice. **J**) Comparison of SA and OH dendrimers for the composition of dendrimer-positive cells within the GL261 tumor. For all statistical analyses, * $p < 0.05$, ** $p < 0.01$, **** $p < 0.0001$. ns: p value ≥ 0.05 was not shown.

behaviors, such as absorption, distribution, metabolism, elimination (ADME), and toxicity [30,48–50]. We next asked how the cell-level distribution of systemically injected dendrimers can be affected by their surface chemistry. Herein, we selected G6 PAMAM dendrimers with succinamic acid (SA), hydroxyl (OH), and amine (NH₂) terminal groups. All three dendrimers showed approximately ~6 nm diameter (number average mean, Fig. S5A). When measured in 1 × PBS, NH₂, OH, and SA dendrimers showed cationic ($\zeta = 32.2 \pm 0.5$ mV), neutral ($\zeta = 5.0 \pm 0.2$ mV), anionic ($\zeta = -22.4 \pm 0.6$ mV) surface charges (Fig. S5B). To trace dendrimers *in vivo*, all three dendrimers were stably labeled with a minimal amount of Cy5 (1% or 5% by wt%) through previously established conjugation chemistry [30] (Fig. S5C–E). We started by systemically injecting all three dendrimers (50 mg/kg) into transgenic mice with established KR158 tumors or age-matched healthy controls. At the dose of 50 mg/kg, NH₂ dendrimers induced significant toxicities that ultimately led to animal death. The high *in vivo* toxicity of systemically administrated NH₂ dendrimers has been reported previously [51]. Our *in vitro* toxicity study based on bone marrow-derived M-MDSCs also showed when the dendrimer dose is ≥ 20 $\mu\text{g/mL}$, NH₂ dendrimers showed significantly higher toxicity than OH and SA dendrimers (Fig. S6A). Therefore, we lowered the dose of NH₂ dendrimers to 10 mg/kg for the following *in vivo* studies.

3.5. NH₂ dendrimers cannot efficiently access M-MDSCs, but can be readily taken up by M-MDSCs

Nanoparticles need to efficiently cross tissue barriers (e.g. the blood vessels and tissue extracellular matrix) before successfully accessing the cells located in the tissue stroma. We determined how dendrimer surface functionality affects their abilities to selectively be endocytosed by M-MDSCs by measuring the percentage of dendrimer-positive M-MDSCs in tissue (% dendrimer+ M-MDSCs). The bone marrow and the tumor are the origin and the destination of M-MDSC recruitment respectively, therefore they were selected as the tissues of interest in this study. We found that the percentage of dendrimer+ M-MDSCs was significantly lower for NH₂ than other dendrimers in the bone marrow of both KR158 tumor-bearing mice and healthy control (Fig. 4A). In the bone marrow, the blood-bone barrier contains fenestrated blood vessels that supply bone with nutrients and transport blood stem cells into circulation. We believe the small sizes of dendrimers (sub 10 nm) enabled them to efficiently cross the blood-bone barrier. However, the confocal images showed that distribution of OH and SA dendrimer were more ubiquitous in the bone marrow compared with the NH₂ dendrimer (Fig. S6B), indicating the NH₂ dendrimer has less capacity to cross the blood-bone barrier compared to OH and SA dendrimers. In the KR158 tumor stroma, NH₂ dendrimers also targeted less M-MDSCs ($12.3 \pm 5.3\%$) than SA ($28 \pm 12.7\%$) and OH dendrimers ($19.0 \pm 6.3\%$) (Fig. 4B). The lower cell-targeting of NH₂ dendrimers was in part due to their lack of ability to cross tissue barriers [30]. Confocal imaging of KR158 tumor sections showed that NH₂ dendrimers were mostly co-localized with the endothelial cells along the blood vessels (Fig. S6C and S7A), indicating the NH₂ dendrimers with strong cationic surface charge were not able to cross the BBTB and other tissue barriers [30]. However, OH and SA dendrimers were able to efficiently cross the BBTB and distribute within the tumor stroma (Fig. S7 D, E, F and G, H, I). We further investigated how dendrimer pharmacokinetics affected their tumor deposition and cell interactions by measuring the plasma concentration of NH₂, SA, and OH dendrimers at 24 h after injection (the timepoint when dendrimer distribution in and uptake were evaluated). Our results showed that at 24 h after injection, the percentage of the injected dose in the plasma was significantly lower for NH₂ dendrimer compared to OH and SA dendrimers (Fig. S6D). It has been reported that the rapid plasma clearance of cationic dendrimer is caused by their avid binding to the vasculature of highly perfused organs [48]. Collectively, we believe that both the faster clearance and the lack of barrier penetration contributed to the lower percentage of M-MDSCs taking up dendrimers in the tissue.

Interestingly, although NH₂ dendrimers were not taken up by many M-MDSCs in the bone marrow, the M-MDSCs that endocytosed NH₂ dendrimers showed similar quantities for tumor-bearing mice and higher quantities of intracellular dendrimers for healthy controls over OH and SA dendrimers (Fig. 4C). Specifically, in the bone marrow of healthy mice, the NH₂ dendrimer (MFI = 1236 ± 453) showed 3.2-fold and 2.7-fold higher M-MDSC-uptake than OH (MFI = 384 ± 15) and SA dendrimers (MFI = 466 ± 33) (Fig. 4D). In the tumor M-MDSCs of KR158 tumor-bearing mice, NH₂ dendrimers also showed slightly higher MFI (MFI = 685 ± 172) than OH (MFI = 442 ± 144) and SA dendrimers (MFI = 595 ± 103) (Fig. 4E, not statistically significant). Given the dose of NH₂ dendrimer is 5-fold lower (10 mg/kg) than OH and SA dendrimers, NH₂ dendrimers demonstrated higher capacity for M-MDSC uptake.

In summary, our data revealed that NH₂ dendrimers do not efficiently cross the tissue barriers. However, they can be readily taken up by M-MDSCs compared to SA and OH dendrimers. This result implies that the cell-mediated delivery can play a critical role in contributing to the NH₂ dendrimer tumor deposition than SA and OH dendrimers.

3.6. M-MDSCs take up SA dendrimers more readily than OH dendrimers

Although SA and OH dendrimers did not show significant differences in their overall tumor deposition (Fig. S8), they did display differential cellular uptake by M-MDSCs. Specifically, in the KR158 tumor, M-MDSCs took up more SA than OH dendrimers (Fig. 4D and E) 24 h after injection. When comparing the MFI of dendrimer-positive M-MDSCs in the bone marrow of tumor-bearing mice, the SA (MFI = 918 ± 173) was 82% higher than OH (MFI = 504 ± 85) (Fig. 4D), while for tumor M-MDSCs, the SA (MFI = 595 ± 103) was 35% higher than OH (MFI = 442 ± 144) (Fig. 4E). In mice that received SA dendrimers, the M-MDSCs compartment and the CX3CR1^{int} compartment (cells that are potentially derived from M-MDSCs) accounted for a higher fraction (30.3%) of the dendrimer-positive cells when compared to mice that received OH dendrimers (20.5%) (Fig. 4F). We further validated the difference between SA and OH dendrimer uptake in the GL261 tumor model. Within the GL261 tumor stroma, M-MDSCs took up more SA and OH dendrimers than other cell subsets (Fig. 4G). Tumor M-MDSCs took up 45% higher SA (MFI = 2437 ± 250) than OH dendrimers (MFI = 1683 ± 245) (Fig. 4H), while bone marrow M-MDSCs took up 40% higher SA (MFI = 1003 ± 175) than OH dendrimers (MFI = 720 ± 264) (Fig. 4I). Similar to the KR158 tumor, in the GL261 tumor of SA dendrimer-injected mice, the M-MDSCs compartment and the CX3CR1^{int} compartment accounted for a higher fraction (65.1%) of dendrimer-positive cells than OH dendrimer injected mice (43.2%) (Fig. 4J). In summary, these results showed that SA dendrimers were more efficiently endocytosed by M-MDSCs than OH dendrimers.

3.7. Dendrimer-associated serum proteins mediate the interactions between dendrimers and M-MDSCs

Given that M-MDSC showed different capacities for endocytosing NH₂, OH, and SA dendrimers *in vivo*, we next sought to determine the mechanism behind the differential uptake by testing the dendrimer uptake in *ex vivo* generated M-MDSCs. Adapted from an established *ex vivo* M-MDSC culturing model [31], we exposed bone marrow cells isolated from CCR2^{REP/WT}CX3CR1^{GFP/WT} transgenic mice to KR158 conditioned media for 5 days. Flow cytometry analysis showed that we can expand the population of CCR2⁺/CX3CR1⁺ cells in the bone marrow from <10% to approximately 59% of the total cells *ex vivo* (Fig. 5A and B). These cells successfully recapitulate the immune suppressive features and the migration pattern of M-MDSCs in the tumor-bearing mice [31]. When these *ex vivo* generated M-MDSCs were exposed to NH₂, OH, and SA dendrimers in a serum-free media at a non-toxic dose of 10 $\mu\text{g/mL}$ (Fig. S6A), a differential uptake of dendrimers was observed. Specifically, the dendrimer uptake was the highest for NH₂, followed by SA,

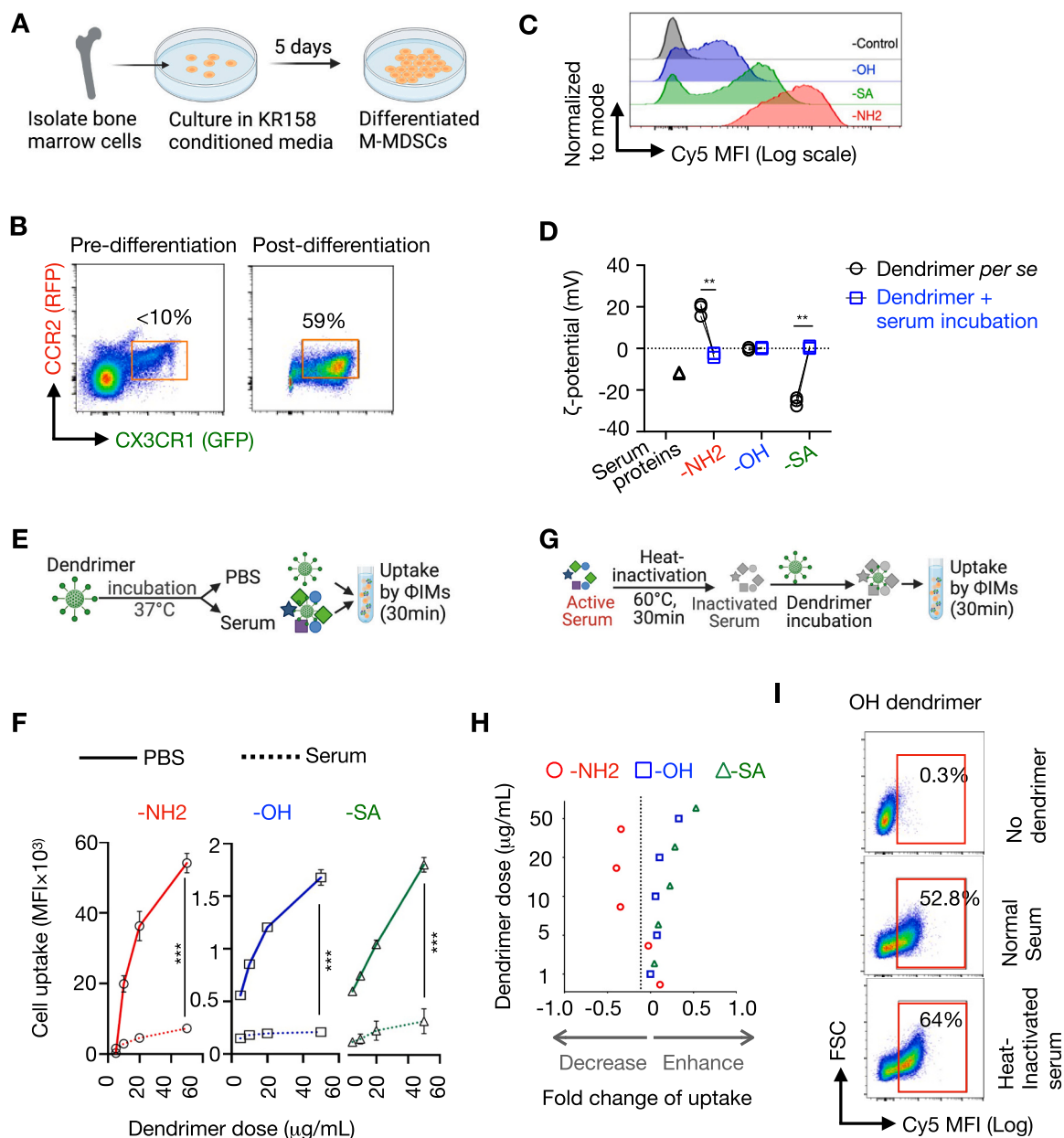


Fig. 5. The serum proteins associated with dendrimers dictate the interaction between dendrimers and M-MDSCs.

A) Schematic illustration shows the generation of M-MDSC from the bone marrow of CCR2^{WT/RFP}CX3CR1^{WT/GFP} transgenic mice. To generate the M-MDSCs, bone marrow cells were isolated and cultured in KR158 conditioned media for 5 days. **B)** Flow cytometry analysis shows that exposure of bone marrow cells to KR158 conditioned media for 5 days enriched the CCR2⁺/CX3CR1⁺ cells (M-MDSCs) from <10% to approximately 59%. **C)** The histogram compares the uptake of OH, SA, and NH₂ dendrimers (indicated by Cy5 MFI) by *ex vivo* generated M-MDSCs in the absence of mouse serum. To generate the plot, M-MDSCs were incubated with dendrimers at room temperature (RT) for 30 min. **D)** Comparison of ζ-potentials (mV) of serum proteins (black triangle) and NH₂, OH, and SA dendrimers before (black circle) and after incubation with mouse serum (blue square). Dendrimers were incubated at 0.86 mg/mL in normal murine serum at 37 °C for 30 min. ζ-potentials (mV) determined using DLS. The experiment was repeated for 3 times (n = 3). **E)** Schematic illustration shows the experiment flow that determines the influence of serum proteins on the dendrimer uptake by M-MDSCs. **F)** The plot based on the experiment flow in (E), which shows dose-dependent dendrimer uptake (indicated by Cy5 MFI) by M-MDSCs after co-incubation with either PBS (solid line) or mouse serum (dotted line) for NH₂ (red, circle), OH (blue, square), and SA (green, triangle) dendrimers. Each data point is an average of 3 independent experiments. **G)** Schematic illustration shows the experiment flow that determines how heat-inactivation of serum affect the uptake of NH₂, OH, and SA dendrimers by M-MDSCs. **H)** The plot based on the experiment flow in (G), which shows the fold change of dendrimer uptake (x-axis) before and after heat-inactivation of mouse serum as a function of dendrimer dose (y-axis). NH₂: red circle, OH: blue square, SA: green triangle. Negative fold change indicates heat inactivation of serum decreased dendrimer uptake. Positive fold change indicates heat inactivation of serum enhance dendrimer uptake. Each data point is an average of 3 independent experiments. **I)** Representative scattered plot shows heat inactivation of mouse serum enhanced the uptake of OH dendrimers by M-MDSCs. **p < 0.01, ***p < 0.005. (For interpretation of the references to color in this figure legend, the reader is referred to the web version of this article.)

and OH dendrimers (Fig. 5C).

Although histologic studies have established that the surface charge of dendrimers can significantly affect their interaction with cells [49,50,52,53], it is now recognized that for systemically injected nanoparticles, it is the serum proteins that are associated with the nanoparticles that dictate nanoparticle interactions with cells [25,54]. To determine how dendrimer-associated serum proteins affect their uptake by M-MDSCs, we first investigated how serum proteins interact with NH₂, OH, and SA dendrimers by evaluating the change of ζ -potential after incubating dendrimers with mouse serum (0.86 mg/mL). Interestingly, after 30 min incubation under 37 °C with mouse serum (ζ -potentials = -11.8 ± 0.37 mV), the original ζ -potentials of NH₂ (32.2 ± 0.5 mV, cationic), OH (5.0 ± 0.2 mV, neutral), and SA (-22.4 ± 0.6 mV, anionic) all became neutral (NH₂: -3.0 ± 1.1 mV; OH: 0.3 ± 0.6 mV; SA: 0.5 ± 0.5 mV) (Fig. 5D), indicating the surfaces of all three dendrimers were masked by the serum proteins. We then exposed all dendrimers either with or without serum incubation to bone marrow-derived M-MDSCs at an escalating dose of 5 μ g/mL to 50 μ g/mL (Fig. 5E). Pre-incubating dendrimers with serum significantly decreased the uptake of all dendrimers in a dose-dependent manner, when compared to dendrimer uptake in non-serum containing PBS (Fig. 5F), or HBSS media (Fig. S9C) indicating that ‘native’ dendrimers and serum protein- ‘coated’ dendrimers interacted with M-MDSCs via different mechanisms. The uptake of NH₂ dendrimers had a greater decrease after serum incubation than the OH and SA dendrimers (Fig. 5F, Fig. S9A,B), indicating the serum protein had a greater influence in mediating the interaction of M-MDSCs with NH₂ dendrimers. Serum proteins can be classified into opsonin (enhance uptake) and dysopsonin (reduce uptake) [54]. To determine the classes of proteins that interacted with dendrimers of different surface functionalities, we incubated dendrimers with either competent ‘active’ serum or ‘heat-inactivated’ mouse serum under 60 °C for 30 min (Fig. 5G), for NH₂ dendrimers, heat-inactivation of serum proteins reduced NH₂ dendrimer uptake in a dose-dependent manner for up to 60% (Fig. 5H, Fig. S9 D–I), indicating serum proteins associated with NH₂ dendrimers actively mediated their uptake by M-MDSCs. However, for both OH and SA dendrimers, heat-inactivation of serum proteins increased their uptake by M-MDSCs up to 24% (OH) and 43% (SA) in a dose-dependent manner (Fig. 5H, Fig. S9 D–I), indicating a different class of serum proteins (potentially dysopsonins) might be associated with OH and SA dendrimers.

Historical studies of the ‘protein corona’ associated with nanoparticles are established on NPs of 20–500 nm size ranges with internally encapsulated payloads [26], such as lipid NPs (LNPs), polymers, and iron oxide NPs. For example, it is well-established systemically administered clinical LNPs selectively target the liver through an endogenous mechanism mediated by Apolipoprotein E (ApoE) – one of the primary components of LNP’s protein [55–57]. Based on this concept, recent studies further determined that apparent pKa and the surface chemistry of LNPs can modulate the composition of the protein corona, which ultimately dictates LNP’s cellular uptake and tissue tropism [57,58]. Different from large NPs, NPs with ultra-small architectures (size range of 1–20 nm), such as dendrimers, gold NPs (AuNPs), and quantum dots, may interact differently with proteins. Compared to large NPs, ultra-small NPs, have sizes similar to proteins and may interact with serum proteins in different stoichiometries and configurations [54]. For example, given the same surface area, AuNPs of 5 nm sizes bind significantly more proteins of all size ranges compared to the larger AuNPs of 80 nm. This indicated the critical role of protein corona for NPs with ultra-small architectures [59]. More importantly, ultra-small NPs such as dendrimers carry payloads on their surfaces. Therefore, the properties of the surface payload will affect how dendrimers interact with M-MDSCs. Here, we used NH₂ and SA dendrimers to represent dendrimers carrying drug molecules of acidic and basic properties and compared them with OH dendrimers (control). We showed that the serum proteins associated with SA and OH dendrimers had a similar influence on their interaction with M-MDSCs, while certain serum

proteins associated with NH₂ dendrimers actively enhance their uptake by M-MDSCs, potentially through receptor-mediated endocytosis. In fact, a recent study showed that NH₂ dendrimers efficiently interact with IgM and trigger complement activation through lectin pathway [60], enhancing their phagocytosis. These *ex vivo* studies provided a basic mechanistic explanation for the differential *in vivo* uptake of NH₂, OH, and SA dendrimers by M-MDSCs. However, to complete the mechanistic study, future research is needed to identify the specific proteins and their cognate receptors on M-MDSCs that mediate the uptake of dendrimers.

4. Conclusion

M-MDSCs suppress the anti-tumor immune response locally at the TME and globally at the lymphoid organs. To address the systemic immune suppression, NPs need to efficiently target these cells both locally and globally. Using the CCR2^{RFP/WT}CX3CR1^{GFP/WT} transgenic mice, that enable direct surveillance of M-MDSCs, we showed that M-MDSCs can infiltrate glioma through peripheral blood in large amounts. Systemically injected hydroxyl dendrimers efficiently target M-MDSCs located in bone marrow, peripheral blood, spleen, and tumor. Within the tumor, M-MDSCs and microglia showed high capacity to endocytose hydroxyl dendrimers and these two cellular compartments accounted for more than half the amount of the hydroxyl dendrimer deposition in the tumor. In the GL261 glioma model, which has a high abundance of infiltrative immune cells, dendrimer showed greater tumor deposition and higher efficiency of M-MDSC-targeting than the KR158 glioma model. We further showed that the recruitment of M-MDSCs from bone marrow to tumor contributed to the tumor deposition of hydroxyl dendrimers. The surface functionality of dendrimers affects their ability to target M-MDSCs *in vivo*. Although amine dendrimers had the highest capacity of being endocytosed by M-MDSCs, they could not access these cells as efficiently as hydroxyl or succinamic acid dendrimers, potentially due to the lack of ability to cross tissue barriers. M-MDSCs took up succinamic acid dendrimers more efficiently than hydroxyl dendrimers. Finally, serum proteins can affect how dendrimers interact with M-MDSCs. The serum proteins associated with amine dendrimers significantly enhanced their uptake by M-MDSCs, while serum proteins associated with hydroxyl and succinamic acid dendrimers slightly reduced their uptake by M-MDSCs. Given that dendrimer-based drug conjugates carry payload on their surfaces, the results of this study indicated that the molecular properties of the selected payload could affect the *in vivo* fate, such as cell- and tissue-targeting of the final dendrimer-drug conjugates.

CRedit authorship contribution statement

Chad A. Littrell: Writing – review & editing, Writing – original draft, Validation, Methodology, Investigation, Formal analysis, Data curation. **Gregory P. Takacs:** Writing – review & editing, Validation, Methodology, Investigation, Formal analysis, Data curation. **Chenikkayala Siva Sankara:** Writing – review & editing, Writing – original draft, Methodology, Formal analysis, Data curation. **Alexandra Sherman:** Methodology, Data curation. **Kai A. Rubach:** Writing – review & editing, Validation, Formal analysis, Data curation. **Julia S. Garcia:** Methodology, Formal analysis, Data curation. **Coral A. Bell:** Validation, Investigation, Formal analysis, Data curation. **Tejashwini Lnu:** Validation, Methodology, Formal analysis, Data curation. **Jeffrey K. Harrison:** Writing – review & editing, Supervision, Resources, Project administration, Methodology, Investigation, Funding acquisition, Conceptualization. **Fan Zhang:** Writing – review & editing, Writing – original draft, Supervision, Resources, Project administration, Investigation, Funding acquisition, Formal analysis, Conceptualization.

Declaration of competing interest

The authors declare no conflicts of interest.

Data availability

Data will be made available on request.

Acknowledgments

The authors are grateful to Ms. Wen Jiang for her help with the tissue sectioning and data validation. We also thank UF Pharmacology & Therapeutics, UF ICBR Cytometry Core (RRID:SCR_019119), and Electron Microscopy Core (RRID:SCR_019146) for providing the cryostat, flow cytometry, and confocal microscopy. This work is supported by the UF Research Opportunity Seed Fund and the American Brain Tumor Association Research Discovery Grant (DG2200050), and National Institute of Health (NS108781).

Appendix A. Supplementary data

Supplementary data to this article can be found online at <https://doi.org/10.1016/j.jconrel.2024.08.003>.

References

- M. Kumar, P. Kulkarni, S. Liu, N. Chemuturi, D.K. Shah, Nanoparticle biodistribution coefficients: A quantitative approach for understanding the tissue distribution of nanoparticles, *Adv. Drug Deliv. Rev.* 194 (2023) 114708. Epub 20230120, <https://doi.org/10.1016/j.addr.2023.114708>. PubMed PMID: 36682420.
- S. Wilhelm, A.J. Tavares, Q. Dai, S. Ohta, J. Audet, H.F. Dvorak, W.C.W. Chan, Analysis of nanoparticle delivery to tumours, *Nat. Rev. Mater.* 1 (5) (2016), <https://doi.org/10.1038/natrevmats.2016.14>. PubMed PMID: WOS: 000377671300001.
- A.C. Anselmo, S. Mitragotri, Cell-mediated delivery of nanoparticles: taking advantage of circulatory cells to target nanoparticles, *J. Control. Release* 190 (2014) 531–541. Epub 20140418, <https://doi.org/10.1016/j.jconrel.2014.03.050>. PubMed PMID: 24747161; PMCID: PMC4142097.
- F. Zhang, Z. Xu, K.J. Jolly, Myeloid cell-mediated drug delivery: From nanomedicine to cell therapy, *Adv. Drug Deliv. Rev.* 197 (2023) 114827. Epub 20230415, <https://doi.org/10.1016/j.addr.2023.114827>. PubMed PMID: 37068659.
- Z. Zhao, A. Ukidve, J. Kim, S. Mitragotri, Targeting strategies for tissue-specific drug delivery, *Cell* 181 (1) (2020) 151–167, <https://doi.org/10.1016/j.cell.2020.02.001> (PubMed PMID: 32243788).
- S.T. Barry, D.I. Gabrilovich, O.J. Sansom, A.D. Campbell, J.P. Morton, Therapeutic targeting of tumour myeloid cells, *Nat. Rev. Cancer* 23 (4) (2023) 216–237. Epub 20230206, <https://doi.org/10.1038/s41568-022-00546-2>. PubMed PMID: 36747021.
- P.F. Wang, S.Y. Song, T.J. Wang, W.J. Ji, S.W. Li, N. Liu, C.X. Yan, Prognostic role of pretreatment circulating MDSCs in patients with solid malignancies: a meta-analysis of 40 studies, *Oncoimmunology* 10 (10) (2018) e1494113. Epub 20180730, <https://doi.org/10.1080/21624402X.2018.1494113> (PubMed PMID: 30288362; PMCID: PMC6169582).
- D. Marvel, D.I. Gabrilovich, Myeloid-derived suppressor cells in the tumor microenvironment: expect the unexpected, *J. Clin. Invest.* 125 (9) (2015) 3356–3364. Epub 20150713, <https://doi.org/10.1172/JCI80005>. PubMed PMID: 26168215; PMCID: PMC4588239.
- D.I. Gabrilovich, Myeloid-derived suppressor cells, *Cancer Immunol. Res.* 5 (1) (2017) 3–8, <https://doi.org/10.1158/2326-6066.Cir-16-0297>. PubMed PMID: WOS:000392240600001.
- Y.J. Kim, S.J. Park, H.E. Broxmeyer, Phagocytosis, a potential mechanism for myeloid-derived suppressor cell regulation of CD8 T cell function mediated through programmed cell Death-1 and programmed cell Death-1 ligand interaction, *J. Immunol.* 187 (5) (2011) 2291–2301, <https://doi.org/10.4049/jimmunol.1002650>. PubMed PMID: WOS:000294059500033.
- A. Dorhoi, N. Du Plessis, Monocytic myeloid-derived suppressor cells in chronic infections, *Front. Immunol.* 8 (2017) 1895. Epub 20180104, <https://doi.org/10.3389/fimmu.2017.01895>. PubMed PMID: 29354120; PMCID: PMC5758551.
- G. Storm, S.O. Belliot, T. Daemen, D.D. Lasic, Surface modification of nanoparticles to oppose uptake by the mononuclear phagocyte system, *Adv. Drug Deliv. Rev.* 17 (1) (1995) 31–48, [https://doi.org/10.1016/0169-409x\(95\)00039-A](https://doi.org/10.1016/0169-409x(95)00039-A). PubMed PMID: WOS:A1995TH26500004.
- F. Alexis, E. Pridgen, L.K. Molnar, O.C. Farokhzad, Factors affecting the clearance and biodistribution of polymeric nanoparticles, *Mol. Pharm.* 5 (4) (2008) 505–515. Epub 20080804, <https://doi.org/10.1021/mp800051m>. PubMed PMID: 18672949; PMCID: PMC2663893.
- J. Deprez, R. Verbeke, S. Meulewaeter, I. Aernout, H. Dewitte, T. Decruy, J. Coudensys, J. Van Duyse, G. Van Isterdael, D. Peer, R. van der Meel, S.C. De Smedt, P. Jacques, D. Elewaut, I. Lentacker, Transport by circulating myeloid cells drives liposomal accumulation in inflamed synovium, *Nat. Nanotechnol.* (2023), <https://doi.org/10.1038/s41565-023-01444-w>. Epub 20230710. PubMed PMID: 37430039.
- J.W. Myerson, P.N. Patel, K.M. Rubey, M.E. Zamora, M.H. Zaleski, N. Habibi, L.R. Walsh, Y.W. Lee, D.C. Luther, L.T. Ferguson, O.A. Marcos-Contreras, P. M. Glassman, L.L. Mazaleuskaya, I. Johnston, E.D. Hood, T. Shuvaeva, J. Wu, H. Y. Zhang, J.V. Gregory, R.Y. Kiseleva, J. Nong, T. Grosser, C.F. Greineder, S. Mitragotri, G.S. Worthen, V.M. Rotello, J. Lahann, V.R. Muzykantov, J. S. Brenner, Supramolecular arrangement of protein in nanoparticle structures predicts nanoparticle tropism for neutrophils in acute lung inflammation, *Nat. Nanotechnol.* 17 (1) (2022) 86–97. Epub 20211118, <https://doi.org/10.1038/s41565-021-00997-y>. PubMed PMID: 34795440; PMCID: PMC8776575.
- T.J. Alban, A.G. Alvarado, M.D. Sorensen, D. Bayik, J. Volovetz, E. Serbinowski, E. E. Mulkearns-Hubert, M. Sinyuk, J.S. Hale, G.R. Onzi, M. McGraw, P.J. Huang, M. M. Grabowski, C.A. Wathen, M.S. Ahluwalia, T. Radivoyevitch, H.I. Kornblum, B. W. Kristensen, M.A. Vogelbaum, J.D. Lathia, Global immune fingerprinting in glioblastoma patient peripheral blood reveals immune-suppression signatures associated with prognosis, *JCI Insight* 3 (21) (2018), <https://doi.org/10.1172/jci.insight.122264>. ARTN e122264. PubMed PMID: WOS:000449225900007.
- P.R. Gielen, B.M. Schulte, E.D. Kers-Rebel, K. Verrijp, S.A.J.F.H. Bossman, M. ter Laan, P. Wesseling, G.J. Adema, Elevated levels of polymorphonuclear myeloid-derived suppressor cells in patients with glioblastoma highly express S100A8/9 and arginase and suppress T cell function, *Neuro-Oncology* 18 (9) (2016) 1253–1264, <https://doi.org/10.1093/neuonc/now034> (PubMed PMID: WOS: 000384005900013).
- F.H. Shand, S. Ueha, M. Otsuji, S.S. Koid, S. Shichino, T. Tsukui, M. Kosugi-Kanaya, J. Abe, M. Tomura, J. Ziogas, K. Matsushima, Tracking of intertissue migration reveals the origins of tumor-infiltrating monocytes, *Proc. Natl. Acad. Sci. USA* 111 (21) (2014) 7771–7776. Epub 20140513, <https://doi.org/10.1073/pnas.1402914111>. PubMed PMID: 24825888; PMCID: PMC4040600.
- R.A. Franklin, W. Liao, A. Sarkar, M.V. Kim, M.R. Bivona, K. Liu, E.G. Pamer, M. O. Li, The cellular and molecular origin of tumor-associated macrophages, *Science* 344 (6186) (2014) 921–925. Epub 20140508, <https://doi.org/10.1126/science.1252510>. PubMed PMID: 24812208; PMCID: PMC4204732.
- J.A. Flores-Toro, D. Luo, A. Gopinath, M.R. Sarkisian, J.J. Campbell, I.F. Charo, R. Singh, T.J. Schall, M. Datta, R.K. Jain, D.A. Mitchell, J.K. Harrison, CCR2 inhibition reduces tumor myeloid cells and unmasks a checkpoint inhibitor effect to slow progression of resistant murine gliomas, *Proc. Natl. Acad. Sci. USA* 117 (2) (2020) 1129–1138. Epub 20191226, <https://doi.org/10.1073/pnas.1910856117>. PubMed PMID: 31879345; PMCID: PMC6969504.
- X. Zhang, L. Detering, D. Sultan, H. Luehmann, L. Li, G.S. Heo, X. Zhang, L. Lou, P. M. Grierson, S. Greco, M. Ruzinova, R. Laforest, F. Dehdashti, K.H. Lim, Y. Liu, CC chemokine receptor 2-targeting copper nanoparticles for positron emission tomography-guided delivery of gemcitabine for pancreatic ductal adenocarcinoma, *ACS Nano* 15 (1) (2021) 1186–1198. Epub 20210106, <https://doi.org/10.1021/acsnano.0c08185>. PubMed PMID: 33406361; PMCID: PMC7846978.
- S. Shen, Y. Zhang, K.G. Chen, Y.L. Luo, J. Wang, Cationic Polymeric Nanoparticle Delivering CCR2 siRNA to Inflammatory Monocytes for Tumor Microenvironment Modification and Cancer Therapy, *Mol. Phys.* 15 (9) (2018) 3642–3653. Epub 20180126, <https://doi.org/10.1021/acs.molpharmaceut.7b00997>. PubMed PMID: 29337566.
- L. Pinton, S. Magri, E. Masetto, M. Vettore, I. Schibuola, V. Ingangi, I. Marigo, K. Matha, J.P. Benoit, A. Della Puppa, V. Bronte, G. Lollo, S. Mandruzzato, Targeting of immunosuppressive myeloid cells from glioblastoma patients by modulation of size and surface charge of lipid nanocapsules, *J. Nanobiotechnol.* 18 (1) (2020) 31. Epub 20200217, <https://doi.org/10.1186/s12951-020-00589-3> (PubMed PMID: 32066449; PMCID: PMC7026969).
- M.P. Plebanek, D. Bhaumik, P.J. Bryce, C.S. Thaxton, Scavenger Receptor Type B1 and Lipoprotein Nanoparticle Inhibit Myeloid-Derived Suppressor Cells, *Mol. Cancer Ther.* 17 (3) (2018) 686–697. Epub 20171227, <https://doi.org/10.1158/1535-7163.MCT-17-0981>. PubMed PMID: 29282300; PMCID: PMC5935575.
- A. Aliyandi, I.S. Zuhorn, A. Salvati, Disentangling Biomolecular Corona Interactions With Cell Receptors and Implications for Targeting of Nanomedicines, *Front. Bioeng. Biotechnol.* 8 (2020) 599454. Epub 20201210, <https://doi.org/10.3389/fbioe.2020.599454>. PubMed PMID: 33363128; PMCID: PMC7758247.
- C. Gunawan, M. Lim, C.P. Marquis, R. Amal, Nanoparticle-protein corona complexes govern the biological fates and functions of nanoparticles, *J. Mater. Chem. B* 2 (15) (2014) 2060–2083. Epub 20140305, <https://doi.org/10.1039/c3tb21526a>. PubMed PMID: 32261489.
- A.M. Caminade, Dendrimers, an Emerging Opportunity in Personalized Medicine? *J. Pers. Med.* 12 (8) (2022) <https://doi.org/10.3390/jpm12081334>. Epub 20220819. PubMed PMID: 36013283; PMCID: PMC9409959.
- K. Liaw, F. Zhang, A. Mangraviti, S. Kannan, B. Tyler, R.M. Kannan, Dendrimer size effects on the selective brain tumor targeting in orthotopic tumor models upon systemic administration, *Bioeng. Transl. Med.* 5 (2) (2020), <https://doi.org/10.1002/btm2.10160> doi: ARTN e10160. PubMed PMID: WOS:000525899400001.
- F. Zhang, P. Mastorakos, M.K. Mishra, A. Mangraviti, L. Hwang, J. Zhou, J. Hanes, H. Brem, A. Olivi, B. Tyler, R.M. Kannan, Uniform brain tumor distribution and tumor associated macrophage targeting of systemically administered dendrimers, *Biomaterials* 52 (2015) 507–516. Epub 20150318, <https://doi.org/10.1016/j.biomaterials.2015.02.053>. PubMed PMID: 25818456; PMCID: PMC41710089.
- E. Nance, F. Zhang, M.K. Mishra, Z. Zhang, S.P. Kambhampati, R.M. Kannan, S. Kannan, Nanoscale effects in dendrimer-mediated targeting of neuroinflammation, *Biomaterials* 101 (2016) 96–107. Epub 20160526, <https://doi.org/10.1016/j.biomaterials.2016.05.044>. PubMed PMID: 27267631; PMCID: PMC5379995.

- [31] G.P. Takacs, C.J. Kreiger, D. Luo, G. Tian, J.S. Garcia, L.P. Deleyrolle, D. A. Mitchell, J.K. Harrison, Glioma-derived CCL2 and CCL7 mediate migration of immune suppressive CCR2(+)/CX3CR1(+) M-MDSs into the tumor microenvironment in a redundant manner, *Front. Immunol.* 13 (2022) 993444. Epub 20230104, <https://doi.org/10.3389/fimmu.2022.993444>. PubMed PMID: 36685592; PMCID: PMC9854274.
- [32] A.F. Haddad, J.S. Young, D. Amara, M.S. Berger, D.R. Raleigh, M.K. Aghi, N. A. Butowski, Mouse models of glioblastoma for the evaluation of novel therapeutic strategies, *Neurooncol. Adv.* 3 (1) (2021), <https://doi.org/10.1093/oaajnl/vdab100>. Epub 20210726. (PubMed PMID: 34466804; PMCID: PMC8403483).
- [33] Z. Chen, X. Feng, C.J. Herting, V.A. Garcia, K. Nie, W.W. Pong, R. Rasmussen, B. Dwivedi, S. Seby, S.A. Wolf, D.H. Gutmann, D. Hambardzumyan, Cellular and Molecular Identity of Tumor-Associated Macrophages in Glioblastoma, *Cancer Res.* 77 (9) (2017) 2266–2278. Epub 20170224, <https://doi.org/10.1158/0008-5472.CAN-16-2310>. PubMed PMID: 28235764; PMCID: PMC5741820.
- [34] K. Greish, G. Thiagarajan, H. Herd, R. Price, H. Bauer, D. Hubbard, A. Burckle, S. Sadekar, T. Yu, A. Anwar, A. Ray, H. Ghandehari, Size and surface charge significantly influence the toxicity of silica and dendritic nanoparticles, *Nanotoxicology* 6 (7) (2012) 713–723, <https://doi.org/10.3109/17435390.2011.604442>. PubMed PMID: WOS:000309751200003.
- [35] T.M. Johanss, J.P. Ward, C.A. Miller, C. Wilson, D.K. Kobayashi, D. Bender, Y. Fu, A. Alexandrov, E.R. Mardis, M.N. Artyomov, R.D. Schreiber, G.P. Dunn, Endogenous Neoantigen-Specific CD8 T Cells identified in two glioblastoma models using a cancer immunogenomics approach, *Cancer Immunol. Res.* 4 (12) (2016) 1007–1015. Epub 20161031, <https://doi.org/10.1158/2326-6066.CIR-16-0156>. PubMed PMID: 27799140; PMCID: PMC5215735.
- [36] D.A. Wainwright, A.L. Chang, M. Dey, I.V. Balyasnikova, C.K. Kim, A. Tobias, Y. Cheng, J.W. Kim, J. Qiao, L. Zhang, Y. Han, M.S. Lesniak, Durable therapeutic efficacy utilizing combinatorial blockade against IDO, CTLA-4, and PD-L1 in mice with brain tumors, *Clin. Cancer Res.* 20 (20) (2014) 5290–5301. Epub 20140401, <https://doi.org/10.1158/1078-0432.CCR-14-0514>. PubMed PMID: 24691018; PMCID: PMC4182350.
- [37] R. Wouters, S. Bevers, M. Riva, F. De Smet, A. Coosemans, Immunocompetent Mouse Models in the Search for Effective Immunotherapy in Glioblastoma, *Cancers (Basel)* 13 (1) (2020), <https://doi.org/10.3390/cancers13010019>. Epub 20201123. PubMed PMID: 33374542; PMCID: PMC7793150.
- [38] D. Chen, S.B. Le, T.E. Hutchinson, A.A. Calinescu, M. Sebastian, D. Jin, T. Liu, A. Ghiaseddin, M. Rahman, D.D. Tran, Tumor treating fields dually activate STING and AIM2 inflammasomes to induce adjuvant immunity in glioblastoma, *J. Clin. Invest.* 132 (8) (2022), <https://doi.org/10.1172/JCI149258> (PubMed PMID: 35199647; PMCID: PMC9012294).
- [39] J.L. Guerriero, Macrophages: The Road Less Traveled, Changing Anticancer Therapy, *Trends Mol. Med.* 24 (5) (2018) 472–489. Epub 20180411, <https://doi.org/10.1016/j.molmed.2018.03.006>. PubMed PMID: 29655673; PMCID: PMC5927840.
- [40] A. Mantovani, F. Marchesi, A. Maleski, L. Laghi, P. Allavena, Tumour-associated macrophages as treatment targets in oncology, *Nat. Rev. Clin. Oncol.* 14 (7) (2017) 399–416, <https://doi.org/10.1038/nrclinonc.2016.217>. PubMed PMID: WOS: 000403682800003.
- [41] F. Klemm, R.R. Maas, R.L. Bowman, M. Kornete, K. Soukup, S. Nassiri, J. P. Brouland, C.A. Iacobuzio-Donahue, C. Brennan, V. Tabar, P.H. Gutin, R. T. Daniel, M.E. Hegi, J.A. Joyce, Interrogation of the microenvironmental landscape in brain tumors reveals disease-specific alterations of immune cells, *Cell* 181 (7) (2020) 1643–1460 e17. Epub 20200528, <https://doi.org/10.1016/j.cell.2020.05.007>. PubMed PMID: 32470396; PMCID: PMC8558904.
- [42] R.L. Bowman, F. Klemm, L. Akkari, S.M. Pyonteck, L. Sevenich, D.F. Quail, S. Dhara, K. Simpson, E.E. Gardner, C.A. Iacobuzio-Donahue, C.W. Brennan, V. Tabar, P.H. Gutin, J.A. Joyce, Macrophage Ontogeny Underlies Differences in Tumor-Specific Education in Brain Malignancies, *Cell Rep.* 17 (9) (2016) 2445–2459. Epub 20161110, <https://doi.org/10.1016/j.celrep.2016.10.052>. PubMed PMID: 27840052; PMCID: PMC5450644.
- [43] M.A. Miller, R. Chandra, M.F. Cuccarese, C. Pfirsche, C. Engblom, S. Stapleton, U. Adhikary, R.H. Kohler, J.F. Mohan, M.J. Pittet, R. Weissleder, Radiation therapy primes tumors for nanotherapeutic delivery via macrophage-mediated vascular bursts, *Sci. Transl. Med.* 9 (392) (2017), <https://doi.org/10.1126/scitranslmed.aal0225> (PubMed PMID: 28566423; PMCID: PMC6681815).
- [44] M.A. Miller, Y.R. Zheng, G.W. Suresh, C. Pfirsche, H. Zope, C. Engblom, R. H. Kohler, Y. Iwamoto, K.S. Yang, B. Askevold, N. Kolishetti, M. Pittet, S.J. Lippard, O.C. Farokhzad, R. Weissleder, Tumour-associated macrophages act as a slow-release reservoir of nano-therapeutic Pt(IV) pro-drug, *Nat. Commun.* (2015) 6. ARTN 8692, <https://doi.org/10.1038/ncomms9692>. PubMed PMID: WOS: 000364937600006.
- [45] E.A. Sykes, Q. Dai, C.D. Sarsons, J. Chen, J.V. Rocheleau, D.M. Hwang, G. Zheng, D.T. Cramb, K.D. Rinker, W.C. Chan, Tailoring nanoparticle designs to target cancer based on tumor pathophysiology, *Proc. Natl. Acad. Sci. USA* 113 (9) (2016) E1142–E1151. Epub 20160216, <https://doi.org/10.1073/pnas.1521265113>. PubMed PMID: 26884153; PMCID: PMC4780626.
- [46] I.N. Eckert, E. Ribecchini, K.J. Jarick, S. Strozniak, S.J. Potter, A. Beilhack, M. B. Lutz, VLA-1 Binding to Collagen IV Controls Effector T Cell Suppression by Myeloid-Derived Suppressor Cells in the Splenic Red Pulp, *Front. Immunol.* 11 (2020) 616531. Epub 20210118, <https://doi.org/10.3389/fimmu.2020.616531>. PubMed PMID: 33584706; PMCID: PMC7873891.
- [47] H.I. Tong, W. Kang, P.M.C. Davy, Y.L. Shi, S. Sun, R.C. Allsopp, Y.A. Lu, Monocyte trafficking, engraftment, and delivery of nanoparticles and an exogenous gene into the acutely inflamed brain tissue - evaluations on monocyte-based delivery system for the central nervous system, *PLoS One* 11 (4) (2016), <https://doi.org/10.1371/journal.pone.0154022> doi: ARTN e0154022. PubMed PMID: WOS: 000374973600036.
- [48] L.M. Kaminskas, B.J. Boyd, C.J. Porter, Dendrimer pharmacokinetics: the effect of size, structure and surface characteristics on ADME properties, *Nanomedicine (London)* 6 (6) (2011) 1063–1084, <https://doi.org/10.2217/nmm.11.67> (PubMed PMID: 21955077).
- [49] L. Albertazzi, L. Gherardini, M. Brondi, S.S. Sato, A. Bifone, T. Pizzorusso, G. M. Ratto, G. Bardi, In vivo distribution and toxicity of PAMAM dendrimers in the central nervous system depend on their surface chemistry, *Mol. Pharm.* 10 (1) (2013) 249–260, <https://doi.org/10.1021/mp300391v>. PubMed PMID: WOS: 000313156100025.
- [50] L.P. Wu, M. Ficker, J.B. Christensen, D. Simberg, P.N. Trohopoulos, S.M. Moghimi, Dendrimer end-terminal motif-dependent evasion of human complement and complement activation through IgM hitchhiking, *Nat. Commun.* 12 (1) (2021), <https://doi.org/10.1038/s41467-021-24960-6> doi: ARTN 4858. PubMed PMID: WOS:000684339800028.
- [51] G. Thiagarajan, K. Greish, H. Ghandehari, Charge affects the oral toxicity of poly (amidoamine) dendrimers, *Eur. J. Pharm. Biopharm.* 84 (2) (2013) 330–334. Epub 20130216, <https://doi.org/10.1016/j.ejpb.2013.01.019>. PubMed PMID: 23419816; PMCID: PMC3860365.
- [52] L. Albertazzi, M. Serresi, A. Albanese, F. Beltram, Dendrimer internalization and intracellular trafficking in living cells, *Mol. Pharm.* 7 (3) (2010) 680–688, <https://doi.org/10.1021/mp9002464> (PubMed PMID: 20394437).
- [53] O.P. Perumal, R. Inapagolla, S. Kannan, R.M. Kannan, The effect of surface functionality on cellular trafficking of dendrimers, *Biomaterials* 29 (24–25) (2008) 3469–3476. Epub 20080522, <https://doi.org/10.1016/j.biomaterials.2008.04.038>. PubMed PMID: 18501424.
- [54] E. Papini, R. Tavano, F. Mancini, Oposonins and dysopsonins of nanoparticles: facts, concepts, and methodological guidelines, *Front. Immunol.* 11 (2020) 567365. Epub 20201012, <https://doi.org/10.3389/fimmu.2020.567365>. PubMed PMID: 33154748; PMCID: PMC7587406.
- [55] V. Francia, R.M. Schifferles, P.R. Cullis, D. Witzigmann, The biomolecular Corona of lipid nanoparticles for gene therapy, *Bioconjug. Chem.* 31 (9) (2020) 2046–2059. Epub 20200831, <https://doi.org/10.1021/acs.bioconjchem.0c00366>. PubMed PMID: 32786370.
- [56] A. Akinc, W. Querbes, S. De, J. Qin, M. Frank-Kamenetsky, K.N. Jayaprakash, M. Jayaraman, K.G. Rajeev, W.L. Cantley, J.R. Dorkin, J.S. Butler, L. Qin, T. Racie, A. Sprague, E. Fava, A. Zeigerer, M.J. Hope, M. Zerial, D.W. Sah, K. Fitzgerald, M. A. Tracy, M. Manoharan, V. Koteliansky, A. Fougerolles, M.A. Maier, Targeted delivery of RNAi therapeutics with endogenous and exogenous ligand-based mechanisms, *Mol. Ther.* 18 (7) (2010) 1357–1364. Epub 20100511, <https://doi.org/10.1038/mt.2010.85>. PubMed PMID: 20461061; PMCID: PMC2911264.
- [57] S.A. Dilliard, Q. Cheng, D.J. Siegwart, On the mechanism of tissue-specific mRNA delivery by selective organ targeting nanoparticles, *Proc. Natl. Acad. Sci. USA* 118 (52) (2021), <https://doi.org/10.1073/pnas.2109256118>. PubMed PMID: 34933999; PMCID: PMC8719871.
- [58] D. Chen, S. Ganesh, W. Wang, M. Amiji, The role of surface chemistry in serum protein corona-mediated cellular delivery and gene silencing with lipid nanoparticles, *Nanoscale* 11 (18) (2019) 8760–8775, <https://doi.org/10.1039/c8nr09855g> (PubMed PMID: 30793730).
- [59] M. Schaffler, M. Semmler-Behnke, H. Sarioglu, S. Takenaka, A. Wenk, C. Schleh, S. M. Hauck, B.D. Johnston, W.G. Kreyling, Serum protein identification and quantification of the corona of 5, 15 and 80 nm gold nanoparticles, *Nanotechnology* 24 (26) (2013) 265103, <https://doi.org/10.1088/0957-4484/24/26/265103> (PubMed PMID: 23735821).
- [60] L.P. Wu, M. Ficker, J.B. Christensen, D. Simberg, P.N. Trohopoulos, S.M. Moghimi, Dendrimer end-terminal motif-dependent evasion of human complement and complement activation through IgM hitchhiking, *Nat. Commun.* 12 (1) (2021) 4858. Epub 20210811, <https://doi.org/10.1038/s41467-021-24960-6> (PubMed PMID: 34381048; PMCID: PMC8357934).